Contribution of molecular dynamics in pNMR for the structural determination of AnV and AnVI complexes in solution

Clovis Poulin-Ponnelle, Magali Duvail, Thomas Dumas, Claude Berthon

▶ **To cite this version:**

HAL Id: hal-03790213
https://hal.umontpellier.fr/hal-03790213

Submitted on 3 Oct 2022

Contribution of Molecular Dynamics in pNMR for the structural determination of An$^\mathrm{V}$ and An$^\mathrm{VI}$ complexes in solution

Clovis Poulin-Ponnelle,[†] Magali Duvail,[*,‡] Thomas Dumas,[†] and Claude Berthon[*,†]

†*LILA, Univ Montpellier, CEA, Bagnols sur Cèze, France*
‡*ICSM, Univ Montpellier, CEA, CNRS, ENSCM, Bagnols sur Cèze, France*

E-mail: magali.duvail@cea.fr; claude.berthon@cea.fr

Abstract

In this study, we propose to use classical molecular dynamics (MD) coupled with ^{1}H NMR spectroscopy to study the conformations of different actinyl An$^\mathrm{VI}$ (An = U, Np, Pu) and An$^\mathrm{V}$ (An = Np) complexes with tetra-ethyl dyglicolamide (TEDGA) ligands in order to have a better representation of such complexes in solution. Molecular dynamics simulations showed its effectiveness in interpreting the experiments by the calculation of geometric factors needed for the determination of magnetic properties of these complexes. We demonstrated that different conformations of the An$^\mathrm{V}$ and An$^\mathrm{VI}$ complexes with TEDGA exist in solution with different coordination modes, which is experimentally confirmed by ^{1}H NMR and EXAFS spectroscopies. Furthermore, MD simulations provide additional insights into the structures of complexes in solution since conformations with fast exchanges, which are not accessible from NMR experiments, have been observed by MD simulations.

1   Introduction

The paramagnetic nuclear magnetic resonance (pNMR) is widely used for structural studies of macro-molecules, particularly in biological systems.[1–3] Some of lanthanide(III) cations have a well-known paramagnetic effect due to their $4f$ free electrons. The coordination of these cations on different protein binding sites induces a modification of the protein nuclei chemical shifts on the NMR spectra, called LIS (Lanthanide Induced Shifts). Because of this chemical shifts modification, paramagnetic $4f$ cations can be used as probes in metalloproteins in order to determine their ternary structure.[4–10]

In this framework, the use of paramagnetic $5f$ actinide (An) cations has been studied for structural determinations of complexes in solution.[11] Interactions between actinides and their ligands are important and useful, particularly in the nuclear fuel research.[12,13] Moreover, in environmental science, the toxicology of actinides can be investigated through the cation-peptide coordination chemistry owing to structural information studies.[14,15] Actinide complexes have been studied with some ligands used in extraction chemistry, such as dicarboxylic acid[11,16,17] and diglycolamide.[18–21] Furthermore, we demonstrated recently that some of these actinide cations, namely at the (V) and (VI) oxidation states, could be good probes for the structural determination in solution.[11,17]

The interaction between unpaired electron of the paramagnetic cation and the nuclear spin of the ligand nucleus i is at the origin of the Actinide Induced Shifts (AIS) and corresponds to the paramagnetic contribution δ^i_{para} in the chemical shift observed on NMR spectra. This contribution is determined by subtracting the diamagnetic counterpart from the chemical shifts of an isostructural complex. The paramagnetic shift δ^i_{para} results from two contributions:

$$\delta^i_{\mathrm{para}} = \delta^i_{\mathrm{c}} + \delta^i_{\mathrm{pc}}, \tag{1}$$

where δ^i_{c} is the contact interaction corresponding to the spin density transmission through the bounds, and δ^i_{pc} is the pseudocontact interaction (also called residual dipolar coupling)

2

which is a through space magnetic interaction between the paramagnetic cation and a nucleus i. This pseudocontact interaction[22] δ_{pc}^i (in ppm) is given

$$\delta_{\text{pc}}^i = \frac{10^6}{12\pi N_A} \left(\Delta\chi_{\text{ax}} \frac{3z^2 - r^2}{r^5} + \Delta\chi_{\text{rh}} \frac{3(x^2 - y^2)}{2r^5} \right), \tag{2}$$

where N_A is the Avogadro constant, $\Delta\chi_{\text{ax}}$ and $\Delta\chi_{\text{rh}}$ are the axial and the rhombic parts of the complex magnetic susceptibility anisotropy, respectively. The terms that multiply $\Delta\chi_{\text{ax}}$ and $\Delta\chi_{\text{rh}}$ are called geometric factors and contain structural information. Indeed, x, y and z are the Cartesian coordinates of the nucleus i with respect to the principal frame of χ centered on the metal ion, and r is the cation - nucleus distance. $\Delta\chi_{\text{ax}}$ and $\Delta\chi_{\text{rh}}$ are defined by

$$\begin{aligned} \Delta\chi_{\text{ax}} &= \chi_{zz} - \frac{\chi_{xx} + \chi_{yy}}{2} \\ \Delta\chi_{\text{rh}} &= \chi_{xx} - \chi_{yy} \end{aligned} \tag{3}$$

where χ_{xx}, χ_{yy} and χ_{zz} are the three components of the complex magnetic susceptibility tensor χ in its main frame. Note that, if a complex has a C_n symmetry (with $n \geq 3$) on the z-axis, by definition $x = y$, therefore the rhombic part in Eq. 2 is equal to zero and the δ_{pc}^i becomes proportional to $\Delta\chi_{\text{ax}}$.

The pseudocontact shift δ_{pc}^i is therefore a real source of structural information because it directly depends on the Cartesian coordinates of the nucleus i. It has been demonstrated that, in the case of actinyl complexes, $\delta_{\text{para}}^i = \delta_{\text{pc}}^i$ because δ_{c}^i becomes negligible after 3 chemical bonds away from the paramagnetic cation.[17] This characteristic makes An^V and An^{VI} cations very interesting probes because of this straight relation between δ_{para}^i and δ_{pc}^i. In this perspective, a recent study on An^{VI} has been performed with 2,6-dipicolinate (DPA) as ligand.[17] In order to determine the χ parameters of the magnetic susceptibility tensor, δ_{pc}^i were determined experimentally by pNMR and geometric factors deduced from XRD structures and by DFT (Density Functional Theory) calculations. To go further in the

3

study of the actinyle χ tensor and its evolution with a ligand modification, An^V and An^{VI} complexes with flexible ligand are studied.

However, in order to have a realistic representation of the dynamics of the systems, static DFT calculations are not sufficient enough. Therefore, classical Molecular Dynamics (MD) coupled with pNMR is widely used to study the structure of macro-molecules containing paramagnetic lanthanide cations.[23–26] Indeed, the structures observed in MD simulations are evaluated by studying variations on the experimental $\delta_{\rm pc}^i$. Note that, the experimental $\delta_{\rm pc}^i$ can also be input parameters for MD simulations to refine the macro-molecule structure.[8,27]

The purpose of this paper is to study flexible actinyle complexes with tetra-ethyl dyglicolamide (TEDGA) as ligand. Herein, in order to explore the different conformations existing in solution and to access the geometric factors needed to determine the χ parameters, classical molecular dynamics simulations coupled with NMR and EXAFS spectroscopies have been performed, since this theoretical method has proven its robustness for studying the actinide-ligand interactions.[28–41]

2 Materials and methods

2.1 Sample preparation

$An^{VI}O_2^{2+}$ aqueous solutions were prepared either by dissolving $U^{VI}O_3$ solid compound in HCl 12 mol L^{-1} or using a stock neptunium and plutonium solutions respectively from Np^V or Pu^{IV} in HNO_3 1 mol L^{-1}. Both cations have been oxidized by adding $Ag^{II}O$ in solution: 1/5 molar ratio for $Np^V/Ag^{II}O$ and 1/10 for $Pu^{VI}/Ag^{II}O$. Vis-NIR spectrophotometer (Agilent Cary 500) allows to check the oxidation states purity. Silver in solution was precipitated with a 1:1 HCl ratio and the resulting white solid AgCl separated from the solution by centrifugation. In order to remove HNO_3, solutions were evaporated under N_2 flow after addition of 12 mol L^{-1} of HCl twice in a row.

For the preparation of $[(CH_3)_4N]_2An^{VI}O_2Cl_4$ compounds, two equivalents of $(CH_3)_4NCl$

(compared to An^{VI}) in HCl 3 mol L^{-1} has been added to $An^{VI}O_2^{2+}$ aqueous solutions prior concentration under N_2 flow. The dry $[(CH_3)_4N]_2An^{VI}O_2Cl_4$ compounds are washed twice with tetrahydrofuran (THF) and again dried under N_2 flow.

Finally, for the preparation of $[An^{VI}O_2(TEDGA)_n]^{2+}$ complexes, $[(CH_3)_4N]_2An^{VI}O_2Cl_4$ compounds have been dissolved in CD_3CN. Solid $AgCF_3SO_3$ has been added with a $[(CH_3)_4N]_2An^{VI}O_2Cl_4$ / $AgCF_3SO_3$ molar ratio of 1/4 and the resulting AgCl precipitate removed by centrifugation. One or two equivalent(s) of TEDGA was/were added to obtain 1:1 $[An^{VI}O_2(TEDGA)]^{2+}$ and 1:2 $[An^{VI}O_2(TEDGA)_2]^{2+}$ complexes, respectively.

For all these complexes, the water/complex concentration ratio has been increased in order to study the effect of the presence of water molecules inside the complexes on the chemical shifts. The water concentration in acetonitrile is 90 mmol L^{-1} (determined by ^1H NMR measurements) and the complex concentration is 30 mmol L^{-1}. Solutions containing the complexes have been diluted until the concentration of complexes reached 2.5 mmol L^{-1} while the concentration of water concentration remained constant.

2.2   NMR spectroscopy

^1H NMR spectra were recorded using 400 MHz Fourier transform spectrometer, Agilent DD2, set up for the study of radioactive samples.[42] Acquisitions and processing were performed with OpenVnmrJ 2.1 software.[43] All spectra of $[An^{VI}O_2(TEDGA)_n]^{2+}$ were recorded at 298 K except fore-mentioned.

The molar magnetic susceptibility χ_M has been calculated for all the paramagnetic complexes by the Evans method.[44] The chemical shift difference $\Delta\delta$ between the ^1H NMR signal of working (t-BuOH in) and reference (t-BuOH out) solutions is proportional to the χ_M value (in m^3 mol^{-1}) according to

$$\chi_M = \frac{3\Delta\delta}{10^3[An]}, \tag{4}$$

where the chemical shift difference corresponds to $\Delta\delta = \delta_{tBuOH+An} - \delta_{tBuOH}$ (in ppm), and

[An] is the actinide concentration in mol L^{-1}. These concentrations have been determined by alpha-particle spectroscopy.

2.3   EXAFS spectroscopy

The Extended X-ray Absorption Fine Structure experiments at the U L_{III}-edge (17.1663 keV) were carried out on the MARS beamline at the SOLEIL synchrotron facility (ring operated at 2.75 GeV in top-up mode at an electron current of 500 mA). The optics of the beamline essentially consists of a Double-Crystal Monochromator (DCM) with a pair of Si(220) crystal. The monochromator second crystal is bent to perform the horizontal X-ray beam collimation. Rejection of higher-order harmonics as well as vertical collimation was achieved with two Pt-coated mirrors under total reflection at 3.1 mRad inserted before and after the DCM. A Camberra 13-element HPGe solid state detector was used for data collection in fluorescence mode. All measurements were recorded in double-layered solution cells (250 μL) specifically designed for radioactive samples at room temperature.[45] The edge position calibration was carried out with a Y foil (17.038 keV) as the first inflection point of its first derivative. Data processing was carried out using the Athena code.[46]

The E_0 energy was set according to the maximum of the absorption edge. The EXAFS signal was extracted by subtracting a linear pre-edge background and a combination of cubic spline functions for atomic absorption background. Pseudo-radial distribution functions (PRDF) were obtained by Fourier transform in $k^3\chi(k)$ between 1.2 and 14 Å^{-1}. The R factor (%) and the quality factor (QF, reduced χ^2) of the fits are provided by the ARTEMIS code.[46]

For the EXAFS data analysis, the U samples fitting procedure was based on molecular dynamics structures, taken so that the first coordination shell distances correspond to the average of the simulation. Theoretical scattering phases and amplitudes were calculated using the FEFF8.4 code[47] from the crystallographic parameters and relevant U-O_{yl}, U-Ligand scattering paths were selected to fit the data according to the TEDGA structure. All fitting

operations were performed in R-space over individual radial distances and corresponding Debye-Waller factors (σ^2) for every considered distance in the first coordination shell.

2.4 Simulation details

Molecular Dynamics (MD) simulations of $[U^{VI}O_2(TEDGA)(H_2O)_x]^{2+}$ and $[U^{VI}O_2(TEDGA)_2]^{2+}$ in an acetonitrile box have been carried out in the NPT ensemble with SANDER20, a module of AMBER20[48] using explicit polarization. Periodic boundary conditions were applied to the simulation box. Long-range interactions were calculated using the particle-mesh Ewald method.[49] Equations of motion were numerically integrated using a 1 fs time step. Systems were equilibrated over at least 100 ps at 298.15 K. Simulation runs were collected every picosecond for a total simulation time of 100 ns.

The rigid POL3 model that takes into account the polarization, was used to describe the water molecules,[50,51] and the acetonitrile molecules were described by a polarizable force field.[52,53] The TEDGA molecules were described by the polarizable force field we developed where the van der Waals parameters have been taken from the polarizable parm99 AMBER force field.[54] The partial atomic charges on the TEDGA molecule have been determined from *ab initio* calculations with Gaussian09[55] (Hartree-Fock level of theory with the 6-31G* basis set) using the RESP procedure.[56,57] As generally done a scaling factor of 0.80 has been applied on the atomic charges in order to not overestimate the polarization.[58] The polarizable force field for the uranyl cation we recently developed was used.[35] All the force fields parameters used for the MD simulations are given in the Supporting Information. Since NMR results showed that the An^{VI} (An = U, Np, Pu) complexes with TEDGA have the same stoichiometries, and since theses cations are known to have almost the same distances in their coordination shell with 2,6-dipicolinate ligands (2.45 - 2.47 Å), which have similar coordinating functions as the TEDGA,[17] we assumed here that the An^{VI} complexes formed with TEDGA are isostrucural. Therefore, only the U^{VI} complexes are simulated by molecular dynamics simulations.

Simulation boxes contain the complex formed, *i.e.*, either the 1:1 or the 1:2 molar ratio UO_2^{2+}:TEDGA, with 300 acetonitrile molecules. To mimic the experimental conditions, three water molecules have been added in the simulation box (experimental concentration in water of 90 mmol L^{-1}, *i.e.*, three water molecules for one complex with a concentration of 30 mmol L^{-1}).

For the structural analysis and the calculations of the geometric factors, trajectories have been centered on the uranium atom using the SANDER module CPPTRAJ.[59]

2.5 χ tensor principal frame determination

By convention,[60] the principal frame of χ is defined such that the χ_{zz} axis corresponds to the direction having the most different magnetic susceptibility value from the two others (χ_{xx} and χ_{yy}). Therefore, χ_{xx} axis is the direction that has the smaller value if χ is prolate ($\chi_{zz} \gg \chi_{yy} > \chi_{xx}$) and the larger value if χ is oblate ($\chi_{zz} \ll \chi_{yy} < \chi_{xx}$).

Otherwise, from Eq. 2, δ_{pc}^i can be expressed as a function of χ_{xx}, χ_{yy} and χ_{zz}:

$$\delta_{pc}^i = \frac{10^6}{12\pi N_A} \left(\chi_{xx} G_x^i + \chi_{yy} G_y^i + \chi_{zz} G_z^i \right), \tag{5}$$

where G terms are the geometric factors of the ligand nuclei. These factors are defined as

$$\begin{aligned} G_x^i &= \frac{3x^2 - r^2}{r^5}, \\ G_y^i &= \frac{3y^2 - r^2}{r^5}, \\ G_z^i &= \frac{3z^2 - r^2}{r^5}. \end{aligned} \tag{6}$$

As shown in Eq. 2, the δ_{pc}^i depends only on the anisotropic parts of the tensor, $\Delta\chi_{ax}$ and $\Delta\chi_{rh}$. Therefore, in order to find the main frame of the χ tensor that contains the isotropic part of the tensor and depending on the χ_{xx}, χ_{yy} and χ_{zz} values, it is necessary to take into
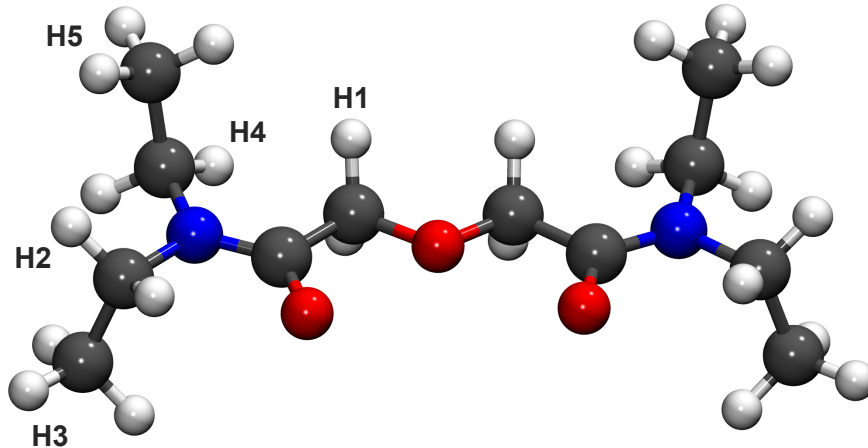
Figure 1: Representation of the TEDGA ligand showing the five different proton groups. For the illustration, the oxygen atoms are colored in red, the nitrogen atoms in blue, the carbon atoms in black, and the hydrogen atoms in white.

account the molar magnetic susceptibility χ_M defined as

$$\chi_M = \frac{1}{3}\chi_{xx} + \frac{1}{3}\chi_{yy} + \frac{1}{3}\chi_{zz}, \tag{7}$$

that gives information on the isotropic part of the χ tensor.

The χ parameters are determined by solving the linear system made of Eq. 5 using a least-squares method[61] considering (i) the geometric factors (G_x^i, G_y^i, G_z^i) of the different proton groups ($i = 1 - 5$) represented in Figure 1 as the matrix, and (ii) the experimental δ_{pc}^i of a paramagnetic complex as a vector. An additional equation (Eq. 7) is added to the linear system, in order to take into account the isotropic part of the χ tensor.

The δ_{pc}^i and χ_M are determined experimentally, and G_x^i, G_y^i and G_z^i of each proton groups are calculated from MD simulations. Then, the χ parameters are determined by solving the linear system for different orientations of the complex in order to find the principal frame of the χ tensor, $i.e.$, χ_{xx}, χ_{yy} and χ_{zz} respecting the convention described before.

The determined χ_{xx}, χ_{yy} and χ_{zz} are used to back-calculate δ_{pc}^i, $i.e.$, $\delta_{pc,calc}^i$, with the geometric factors by solving Eq. 5. The Q_{pc} factor,[62] which corresponds to the quadratic error between the back-calculated δ_i and the experimental δ_i, is used to evaluate the accuracy

of the linear system resolution

$$Q_{pc} = \sqrt{\frac{\sum(\delta^i_{pc,exp} - \delta^i_{pc,calc})^2}{\sum(\delta^i_{pc,exp})^2}}. \tag{8}$$

The lower the Q_{pc} is, the better the resolution of the equations system is.

3 Structural properties of the complexes

3.1 NMR spectroscopy

Tetra-ethyl diglycolamide (TEDGA) ligand has five equivalent proton groups corresponding to five different signals on the ^{1}H NMR spectrum (Fig. 1). We assumed that adding one or two equivalents of TEDGA lead to the formation of An:TEDGA or An:TEDGA$_2$, respectively, that is confirmed since the NMR spectra do not show peaks corresponding to free TEDGA (Figs. S2 - S4). It can be noted here that the signal of the Np^V 1:1 complex is not observed. Indeed, the addition of one equivalent of TEDGA leads to the dismutation of the cation (Np^{IV} + Np^V + Np^{VI}). The Np^V:TEDGA$_2$ complex is nevertheless obtained by the addition of at least two equivalents of TEDGA.

Proton δ^i_{pc} of all the paramagnetic complexes determined by subtraction of the chemical shift from the diamagnetic isostructural counterpart (uranyl complexes, Tab. S6) are given in Table 1. For the same proton group, the δ^i_{pc} values are very close for both Np^{VI} complexes (difference less than 2%), except for the H3 proton group (12%). Concerning the Pu^{VI} complexes, δ^i_{pc} are globally close with variations between 4 and 12%. For the Np^V complex, the δ^i_{pc} values are very close to that of [Pu^{VI}O$_2$(TEDGA)$_2$]$^{2+}$ (difference less than 5% except for the H3 proton group where the difference is 18%), due to their isoelectronic configuration $5f^2$. Moreover, the magnetic susceptibilities χ_M determined with the Evans method (Figs. S5 - S9) for all the paramagnetic complexes, are presented in Table 1. As already observed for δ^i_{pc} values, the χ_M of the complexes are close for a given cation.

Table 1: Experimental ^{1}H δ_{pc}^i of $[\mathrm{An^{VI}O_2(TEDGA)(H_2O)}_x]^{2+}$ and $[\mathrm{An^{VI}O_2(TEDGA)_2}]^{2+}$ complexes with An = Np, Pu and $[\mathrm{Np^{V}O_2(TEDGA)_2}]^+$ in CD_3CN solution at 298 K and 30×10^{-3} mol L^{-1} of An.

Complex	$\delta_{\mathrm{H1}}{}^a$	$\delta_{\mathrm{H2}}{}^a$	$\delta_{\mathrm{H3}}{}^a$	$\delta_{\mathrm{H4}}{}^a$	$\delta_{\mathrm{H5}}{}^a$	$\chi_{\mathrm{M}}{}^b$
$[\mathrm{Np^{VI}O_2(TEDGA)(H_2O)}_x]^{2+}$	-17.76	-11.80	-6.38	-6.72	-4.06	3.63
$[\mathrm{Np^{VI}O_2(TEDGA)_2}]^{2+}$	-17.62	-11.70	-5.63	-6.77	-4.08	3.85
$[\mathrm{Pu^{VI}O_2(TEDGA)(H_2O)}_x]^{2+}$	-52.24	-36.61	-19.50	-21.85	-12.27	9.56
$[\mathrm{Pu^{VI}O_2(TEDGA)_2}]^{2+}$	-46.50	-35.32	-17.07	-19.88	-11.49	9.53
$[\mathrm{Np^{V}O_2(TEDGA)_2}]^{+}$	-47.75	-37.07	-20.18	-20.12	-11.46	8.73

^{a} in ppm; ^{b} 10^{-8} m^3 mol^{-1}.

In order to study the effect of water molecules inside the complexes on the chemical shift, NMR spectra of the complexes with different water / complex ratio were recorded (Fig. 2).

In the case of the $[\mathrm{U^{VI}O_2(TEDGA)(H_2O)}_x]^{2+}$ solution, the dilution does not affect the chemical shifts of the complex (Fig. 2.a). Indeed, water molecules are in fast chemical exchange between the complex first coordination sphere and the bulk (acetonitrile). Therefore, the water chemical shift decreases and the peak becomes thinner as the concentration of the complex decreases and the amount of free water increases.

As shown in the ^{1}H NMR peaks of the two Np^{VI} complexes (noted 1:1 and 1:2 for $[\mathrm{Np^{VI}O_2(TEDGA)(H_2O)}_x]^{2+}$ and $[\mathrm{Np^{VI}O_2(TEDGA)_2}]^{2+}$, respectively), it is only possible to distinguish the H2 and H3 proton groups peaks because H1, H4 and H5 proton groups have very close chemical shifts for both complexes (Fig. 2.b). For the H2 and H3 proton groups of the $[\mathrm{Np^{VI}O_2(TEDGA)(H_2O)}_x]^{2+}$ complex, the chemical shifts increase and the peaks become broader as the complex concentration decreases. However, it is not the case for those of the $[\mathrm{Np^{VI}O_2(TEDGA)_2}]^{2+}$ complex which remain constant. Chemical shifts of the H1, H4 and H5 proton groups also increase with the decreasing of the complex concentration. This is accompanied by the apparition of a shoulder for the H1 and H4 proton groups (at 12.05 and 3.15 ppm) and the vanishing of the shoulder observed for the H5 proton group (at 2.65 ppm), corresponding to the $[\mathrm{Np^{VI}O_2(TEDGA)_2}]^{2+}$ chemical shift.

Similarly to the Np^{VI} complexes, the chemical shifts of the $[\mathrm{Pu^{VI}O_2(TEDGA)(H_2O)}_x]^{2+}$
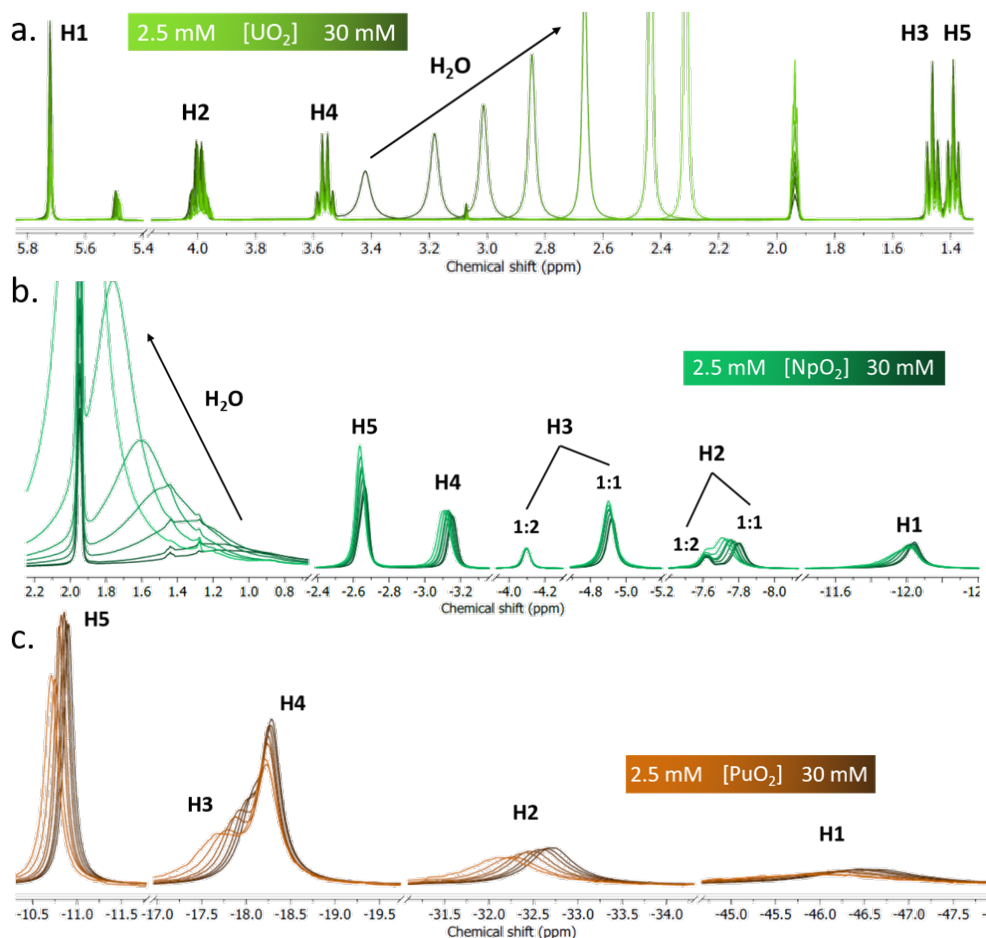
Figure 2: ^{1}H NMR spectra of 1:1 An^{VI}:TEDGA complexes with An = (a) U, (b) Np, and (c) Pu, for different actinyl concentrations in CD$_3$CN (from 2.5 in light color to 30 mmol L^{-1} in dark color). All the spectra are normalized with respect to the complex concentration and recorded at room temperature.

complex increase and the corresponding peaks become broader when the concentration of water increases compared to the complex one (Fig. 2.c). Indeed, the chemical shifts increase between 0.2 and 1 ppm for dilutions of the complex ranging from 30 to 2.5 mmol L^{-1}.

Since this phenomenon is not observed for the $[U^{VI}O_2(TEDGA)(H_2O)_x]^{2+}$ complex, U^{VI} being a diamagnetic cation, we can conclude that this is the presence of a paramagnetic cation, namely Pu^{VI} or Np^{VI}, that induces the modification of the chemical shifts, *i.e.*, when a magnetic anisotropy of the cation exists. This feature allows to highlight any geometry changes through the chemical shift variations in accordance with Eq. 5.

The change in the complex structure linked to the amount of water in solution is cer-

tainly due to different stoichiometries of the complex involving water molecules in the first coordination sphere. In order to observe such a change, an equilibrium between at least two conformations of the 1:1 complex might be observed. Nevertheless, in order to observe a signal splitting, the exchange between these conformations must be slow at NMR time scale (lower than 0.1 s). Unfortunately, at 233 K (near to the acetonitrile melting point) conformations are still in fast exchange, therefore, no signal splitting was observed.

3.2 Molecular Dynamics simulation

MD simulations of uranyl complexes with one and two TEDGA molecules in acetonitrile have been performed in order to access structural properties of the different complexes formed in solution and are required for the calculation of the geometric factors. As mentioned above, three water molecules have been added in order to mimic the experimental conditions.

3.2.1 $[U^{VI}O_2(TEDGA)_2]^{2+}$ complex

During the simulation, we observed two different conformations of the $[U^{VI}O_2(TEDGA)_2]^{2+}$ complex, *i.e.*, either five- or six-coordinated. The main conformation, that corresponds to 88% of the total simulation time, is the five-coordinated one, with the ether oxygen atom of one TEDGA molecule not bonded to the uranyl cation in its first coordination sphere (Fig. 3.a). Furthermore, both ether oxygen atoms are coordinated to the uranyl cation, leading to a six-coordinated complex (Fig. 3.b). This conformation corresponds to the remaining simulation time, that is, 12% of the simulation time. The average life-time of the two conformations have been determined by the direct method of Impey et al.[63] by fitting the numbers of conformation $n(t)$ as a function of the life-time t (Fig. S10). Here, a minimum time parameter ($t^* = 2$ ps) that defines a real "exchange" has been introduced for the fit, as generally done.[64] This procedure gives an average life-time τ of 33.5 ps for the five-coordinated conformation, whereas it is only 3.2 ps for the six-coordinated conformation. Note that, when the ether oxygen atom is not bonded to the uranyl cation, it is located above
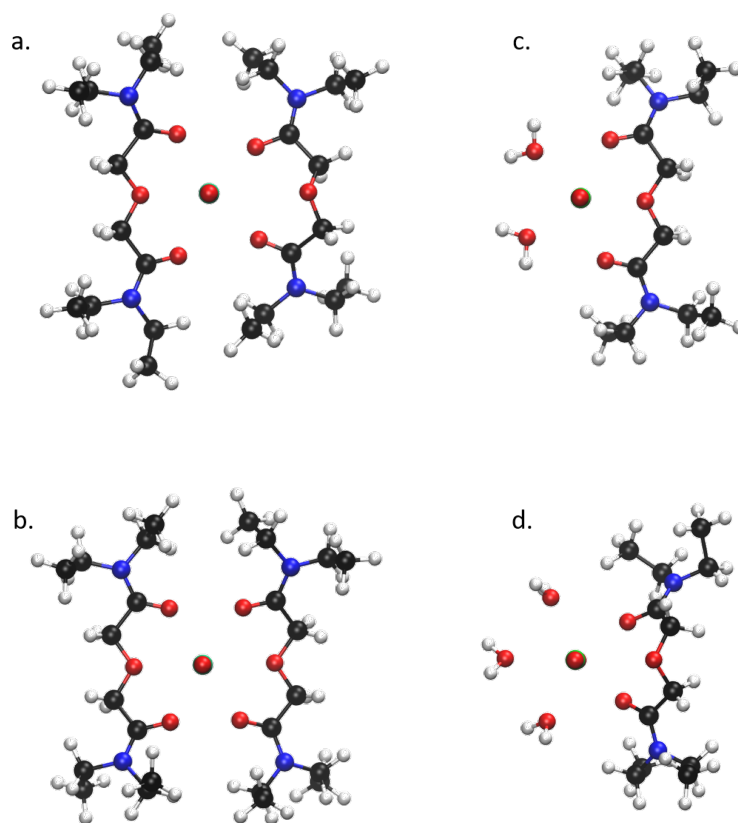
13

Figure 3: Snapshots issued from MD simulations showing the top view of the (a) five- and (b) six-coordinated $[U^{VI}O_2(TEDGA)_2]^{2+}$ complexes, the (c) $[U^{VI}O_2(TEDGA)(H_2O)_2]^{2+}$ and the (d) $[U^{VI}O_2(TEDGA)(H_2O)_3]^{2+}$ complexes. For the illustration, the uranium atoms are colored in green, the oxygen atoms in red, the nitrogen atoms in blue, the carbon atoms in black, and the hydrogen atoms in white.

or below the equatorial plane (Fig. 4) showing the flexibility of the TEDGA ligand.

3.2.2 $[U^{VI}O_2(TEDGA)(H_2O)_x]^{2+}$ complex

As already mentioned, in the case of the $[U^{VI}O_2(TEDGA)(H_2O)_x]^{2+}$ complex, water molecules are present in the uranyl first coordination sphere. During the simulation, two different conformations are observed, both five-coordinated: one with two water molecules, the ether and the two amide oxygen coordinated ($[U^{VI}O_2(TEDGA)(H_2O)_2]^{2+}$), called 2W (Fig. 3.c), and one with three water molecules and only the two amide oxygen coordinated ($[U^{VI}O_2(TEDGA)(H_2O)_3]^{2+}$)
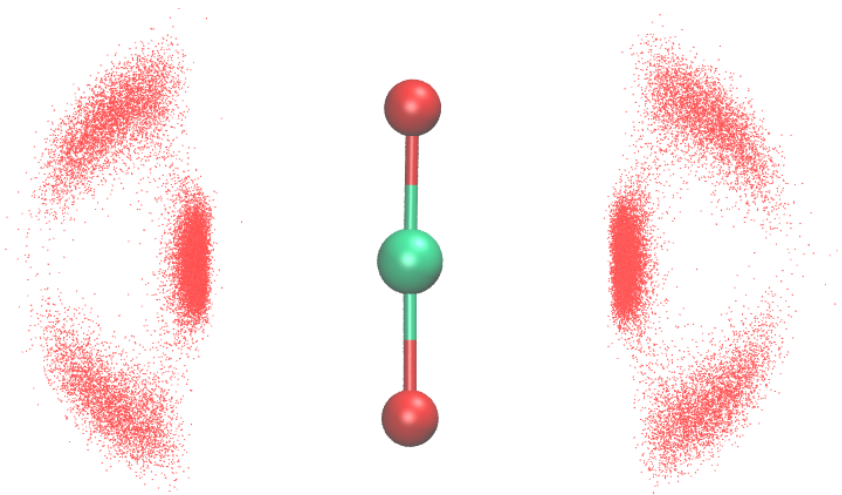
Figure 4: Representation of the positions of the ether oxygen atoms (red points) of the TEDGA molecules during the MD simulations for the $[U^{VI}O_2(TEDGA)_2]^{2+}$ complex. For the illustration, the same colors as in Figure 3 are used.

called 3W (Fig. 3.d). It should be noted here that since only one uranyl cation is present in the MD simulation box, these two conformations correspond to the arrival / departure of one water molecule in / from the uranyl first coordination sphere.

3.3   EXAFS spectroscopy

The k^3-weighted EXAFS spectra at the uranium L_3 edge and the corresponding Fourier transforms (FT) are presented in Figure 5, where the adjusted spectra, based on geometries issued from MD structures, are presented in red. All the metrics parameters are presented in Table 2. The comparison between the radial distribution functions issued from MD simulations and calculated from the EXAFS metrics parameters are presented in Figure S11.

The Fourier transforms of the $[U^{VI}O_2(TEDGA)_2]^{2+}$ EXAFS spectra show a first large peak characteristic of the U-Oyl bond[35] at $R - \phi = 1.37$ Å (Fig. 5.a-b). Then, the next peak, which is double and located at $R - \phi$ around 2 Å, is the contribution of the first coordination sphere, with the amide (Oa) and ether (Oe) oxygen atoms. The contribution of the amide (Ca) and ether (Ce) carbon atoms participate to the peaks located at $R - \phi$

15
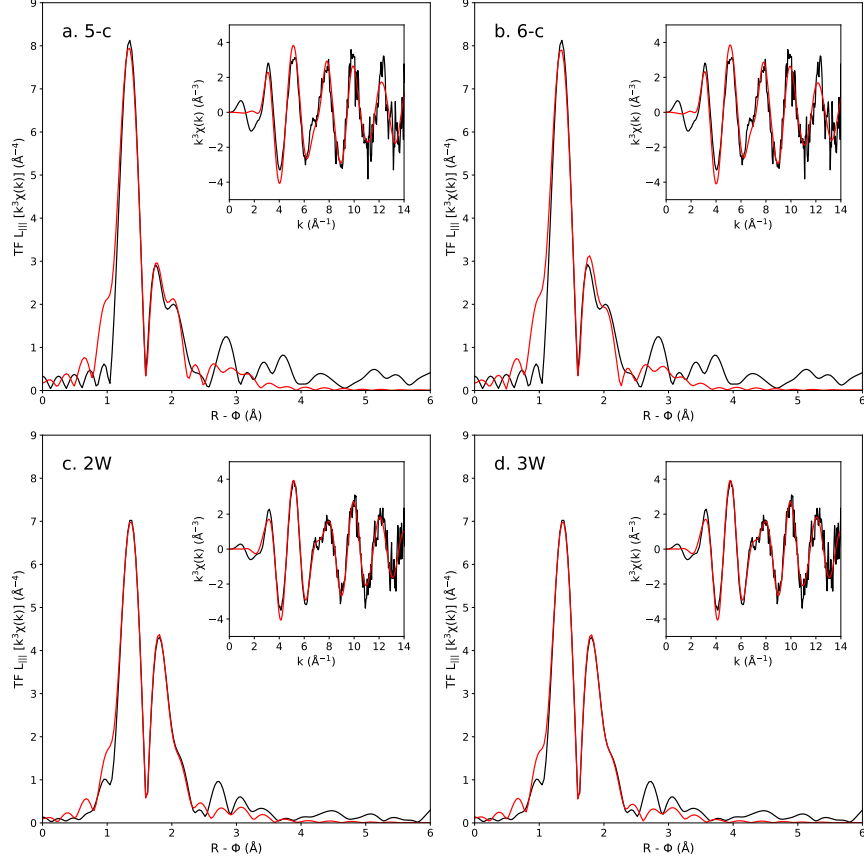
Figure 5: k^3-weighted EXAFS spectra and Fourier transforms (FT) obtained from the k^3-weighted EXAFS spectra for a k range of 1.2 to 14 Å^{-1} determined experimentally (black line) and corresponding fit (red line) for the $[U^{VI}O_2(TEDGA)_2]^{2+}$ complex: (a) and (b) correspond to the five- and six-coordinated conformations, respectively; and the $[U^{VI}O_2(TEDGA)_2]^{2+}$ complex: (c) and (d) correspond to the 2W and 3W conformations, respectively.

around 2.8 Å together with the U-Oyl Multiple Scattering signal.

First, the fit has been performed with the six-coordinated conformation (Tab. 2), corresponding to a 6-c structure from MD simulations: four amide oxygen atoms (Oa) and two ether oxygen atoms (Oe) in the uranyl first coordination sphere. The coordination number N is fixed for the different diffusion paths, and the difference of distances between the U-Oa and U-Oe diffusion paths is constrained to the 0.08 Å MD distance (otherwise the fit gives an U-Oe distance of 2.29 Å which is too small compared to the MD structure). This fit procedure provides very large Debye-Waller factor for U-Oe scattering path ($\sigma^2 = 0.801$ Å^2 for $R = 2.51$ Å and $N = 2$), meaning that the U-Oe contribution is dampened, due to the

Table 2: Best fit parameters calculated from EXAFS spectroscopy and MD simulations.

Complex Conformation	Diffusion paths	N^a	R^b (fit)	σ^{2c} (fit)	R^b (MD)	σ^{2c} (MD)
$[U^{VI}O_2(TEDGA)_2]^{2+}$	U-Oyl	2	1.76 ± 0.00	0.003 ± 0.001	1.77	0.001
six-coordinated	U-Oa	4	2.43 ± 0.01^e	0.012 ± 0.002	2.49	0.008
$R_f = 4.3\%$, $S_0^2 = 1.11$	U-Oe	2	2.51 ± 0.02^e	$0.801 \pm -$	2.57	0.012
$\Delta E^0 = 0.65$ eV	U-Ca	4	3.43 ± 0.03	0.009 ± 0.003	3.44	0.007
	U-Oyl^d	6	3.52 ± 0.01	0.006 ± 0.001	-	-
$[U^{VI}O_2(TEDGA)_2]^{2+}$	U-Oyl	2	1.76 ± 0.00	0.003 ± 0.001	1.77	0.001
five-coordinated	U-Oa	4	2.40 ± 0.02^f	0.018 ± 0.004	2.41	0.005
$R_f = 3.9\%$, $S_0^2 = 1.07$	U-Oe	1	2.45 ± 0.02^f	0.005 ± 0.002	2.46	0.005
$\Delta E^0 = 0.04$ eV	U-Ca	4	3.41 ± 0.02	0.008 ± 0.003	3.36	0.005
	U-Oyl^d	6	3.52 ± 0.00	0.006 ± 0.001	-	-
$[U^{VI}O_2(TEDGA)(H_2O)_2]^{2+}$	U-Oyl	2	1.78 ± 0.00	0.002 ± 0.000	1.77	0.001
2W conformation	U-Oa	2	2.47 ± 0.01	0.001 ± 0.001	2.46	0.006
$R_f = 4.3\%$, $S_0^2 = 0.85$	U-Oe	1	2.47 ± 0.00^g	0.018 ± 0.021	2.48	0.006
$\Delta E^0 = 3.29$ eV	U-Ow	2	2.34 ± 0.01	0.001 ± 0.001	2.38	0.003
	U-Oyl^d	6	3.56 ± 0.00	0.004 ± 0.000	-	-
$[U^{VI}O_2(TEDGA)(H_2O)_3]^{2+}$	U-Oyl	2	1.77 ± 0.00	0.002 ± 0.000	1.78	0.001
3W conformation	U-Oa	2	2.48 ± 0.01	0.001 ± 0.001	2.44	0.005
$R_f = 4.4\%$, $S_0^2 = 0.82$	U-Ow	3	2.35 ± 0.01	0.003 ± 0.001	2.42	0.004
$\Delta E^0 = 3.16$ eV	U-Oyl^d	6	3.55 ± 0.00	0.004 ± 0.000	-	-

^{a} Number of atoms (fixed); ^{b} Distance in Å; ^{c} Debye-Waller factor in Å^2; ^{d} Multiple Scattering path. ^{e} Variation are constrained in a 0.08 Å range of distances between the U-Oa and U-Oe distances; ^{f} Variation are constrained in a 0.05 Å range of distances between the U-Oa and U-Oe distances; ^{g} The U-Oe distance is constrained to be higher than the U-Oa distance;

absence of the Oe atoms at this distance.

The second fit procedure was therefore performed with a five-coordinated conformation issued from MD simulations with four amide oxygen atoms (Oa) and one ether oxygen atom (Oe) in the uranyl first coordination sphere. As already done for the first fitting procedure, the coordination number N is fixed for the different diffusion paths and the distance variation between the U-Oa and U-Oe diffusion paths is constrained to 0.05 Å, otherwise the U-Oe distance fitted would be 2.86 Å which is too high compared to the five-coordinated conformation obtained from MD simulations. However, the Debye-Waller factor

of ether oxygen atoms determined using such procedure ends up to be small ($\sigma^2 = 0.005$ Å^2) compared to amide oxygen ($\sigma^2 = 0.018$ Å^2) while a higher Debye-Waller factor for the U-Oe diffusion path would be expected considering the transition between both conformations.

For both fitting procedures which consider no water molecules in the $[U^{VI}O_2(TEDGA)_2]^{2+}$ first coordination sphere, none of the observed conformations (strictly five- or six-coordinated) allow to correctly reproduce the double peak on the FT corresponding to the first coordination shell (1.6 Å $< R - \phi <$ 2.3 Å), and the one at $R - \phi =$ 2.7 Å. This means that experimentally, the sample does not contain the complex exclusively in one of these conformations. Therefore, the EXAFS signal measured is likely an average signal corresponding to the equilibrium between the five- and the six-coordinated conformations since it has been shown by NMR experiments that both TEDGA ligands are complexed to the uranyl cation. This is in agreement with the results from MD simulations on $[U^{VI}O_2(TEDGA)_2]^{2+}$ complex showing two different conformations in equilibrium. Indeed, EXAFS spectra have been calculated from MD simulations for these two conformations by using FEFF 8.4[47] (Fig .S12). The same FT shapes are observed for $R - \phi$ between 1.6 Å and 2.3 Å for both the experimental and theoretical EXAFS signals. The intensity of the experimental signal is nevertheless lower than the theoretical one, which reflects a higher disorder (σ^2) in the first coordination shell. Furthermore, comparing the EXAFS signals with the ones issued from MD simulations allows to determine that the 6-c conformation contributed to 62% of the total EXAFS signal, whereas it is 38% for the 5-c conformation (Fig. S12).

As already observed for the $[U^{VI}O_2(TEDGA)_2]^{2+}$ complex, the Fourier transforms of the $[U^{VI}O_2(TEDGA)(H_2O)_x]^{2+}$ (2W conformation) EXAFS spectra show a first large peak corresponding to the oxygen of the U-Oyl bond (Fig. 5.c-d) . The peak centered at $R - \phi$ = 1.8 Å with a shoulder at 2.1 Å, is the contribution to the first coordination sphere of the amide (Oa), the ether (Oe), and the water (Ow) oxygen atoms. The contribution of the amide (Ca) and ether (Ce) carbon atoms are visible on the others peaks again close to the U-Oyl Multiple Scattering path.

The first adjustment has been performed for the 2W conformation of the uranyl complex, with TEDGA molecules coordinated by three oxygen atoms, typically two Oa atoms and one Oe atom (Tab. 2). The coordination numbers are fixed and the U-Oe distance is constrained in such a way that it is higher than the U-Oa distance, otherwise the U-Oe distance fitted would be 1.80 Å, which is to small. The adjustment reproduces the experimental spectrum with a good agreement. The TEDGA amide oxygen atoms are found at the same distance than the ether oxygen atom (2.47 Å), which is close to the MD distances (2.46 and 2.48 Å for respectively the U-Oa and U-Oe distances). Furthermore, water oxygen atoms are located at 2.34 Å from the cation, that is close to the distance values determined by MD simulations (2.38 Å).

Comparing the theoretical EXAFS signals of the 2W and 3W conformations obtained from the MD simulations, and the experimental ones, we observed that the FT shape of the 2W conformation is in better agreement between 1.6 Å and 2.3 Å than the FT shape of the 3W conformation (Fig. S12). Furthermore, fitting the experimental signal using a linear combination of both the 2W and 3W signals allows to conclude that the 2W conformation contributes to 100% of the total EXAFS signal.

4   Orientation of the χ tensor

4.1   Determination of the χ tensor principal frame

In the case of conformations having a C_n symmetry (with $n \geq 3$), we could have used an axial χ tensor with no rhombic part. However, here, none of these complex conformations have a $C_{n \geq 3}$ symmetry, so it is not possible, *a priori*, to use such an approximation. Therefore, the equatorial χ components will be taken into account.

In order to determine the χ tensor principal frame, the geometric factors G_x^i, G_y^i and G_z^i are calculated by extracting x^i, y^i and z^i of each proton for each frame (Eq. 6). Geometric factors are then averaged in each five equivalent proton groups. This calculation is repeated
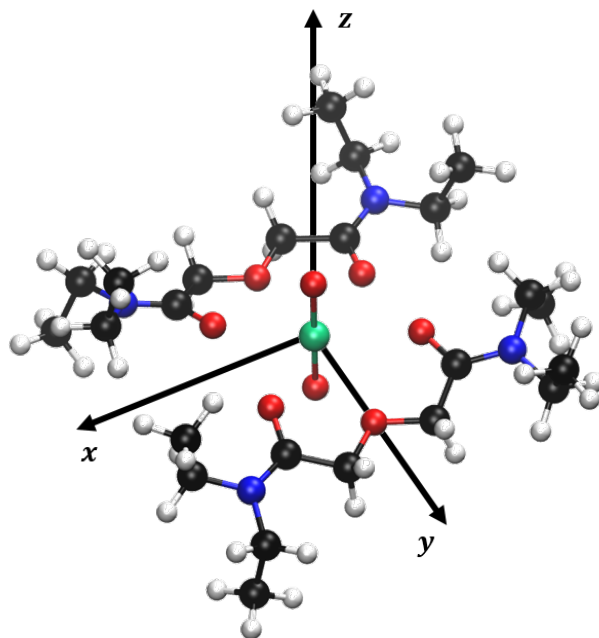
Figure 6: Orientation of the principal axes of the χ tensor shown for the $[\mathrm{U^{VI}O_2(TEDGA)_2}]^{2+}$ complex. For the illustration, the same colors as in Figure 3 have been used.

for the different complex orientations. The linear system, as given by Eqs. 5 and 7, is resolved with the experimental χ_M and δ^i_{pc} values determined for the $[\mathrm{An^{VI}O_2(TEDGA)(H_2O)_x}]^{2+}$, $[\mathrm{An^{VI}O_2(TEDGA)_2}]^{2+}$ and $[\mathrm{Np^VO_2(TEDGA)_2}]^+$ complexes (An = Np, Pu), and the G^i_x, G^i_y and G^i_z determined from MD simulations. The orientation that corresponds to the χ tensor main frame, $i.e.$, that satisfied the convention described before, is found with the χ_{zz} axis corresponding to the U-Oyl for all the complex conformations. The y-axis is passing through the center of mass of one of the TEDGA, $i.e.$, the ether oxygen atom, and the x-axis corresponds to the axis splitting the two TEDGA molecules (for the $[\mathrm{An^{VI}O_2(TEDGA)_2}]^{2+}$ complexes) or the TEDGA and the water molecules (for the $[\mathrm{An^{VI}O_2(TEDGA)(H_2O)_x}]^{2+}$ complexes) (Fig. 6). Regarding the $[\mathrm{Np^{VI}O_2(TEDGA)_2}]^{2+}$ complex and the 3W conformation of $[\mathrm{An^{VI}O_2(TEDGA)(H_2O)_x}]^{2+}$ complex, this is the x-axis that passes through the center of mass of one of the TEDGA molecule.

All the frames of molecular dynamics simulations were rotated (in order to follow the

convention $\chi_{zz} \gg \chi_{yy} > \chi_{xx}$) to be in the orientation described before, *i.e.*, the U-Oyl bond orientated along the z-axis, and the y-axis (or x-axis depending the complex) passing through the center-of-mass of one TEDGA molecule. Therefore, the complex is placed on the principal frame of the χ tensor, allowing to use Equation 6 for the calculation of the geometric factors.

4.2   Geometric factor distributions

Once the complex reoriented for all the MD simulation frames with respect to the principal frame of the χ tensor, the new geometric factors G_x, G_y and G_z are recalculated by extracting x, y and z of each proton for each frame (Eq. 6), and then averaged for the five equivalent proton groups. Note that, for the $[U^{VI}O_2(TEDGA)_2]^{2+}$ complex, the 5-c and 6-c conformation geometric factors have been calculated over 87695 and 12305 configurations, respectively, whereas for the $[U^{VI}O_2(TEDGA)(H_2O)_x]^{2+}$ complex, we used 30581 and 69419 configurations for the 2W and 3W conformations.

The distributions of the G_x^i, G_y^i and G_z^i geometric factors, as well as all the possible positions of the protons around the cation, are presented in Figure 7 for the five- (5-c) and six-coordinated (6-c) conformations of the $[U^{VI}O_2(TEDGA)_2]^{2+}$ complex, and the 2W and 3W conformations of the $[U^{VI}O_2(TEDGA)(H_2O)_x]^{2+}$ complex. These distributions have different shapes, depending directly on the variation of the r distance between the cation and the nucleus (Eq. 6). Indeed, as an example, the H4 proton group has a very narrow range of r distances, so the distribution of the H4 G_z factors is narrow too. On the contrary, the protons belonging to the H3 group are more diffuse with a wide range of r distances, so the H3 G_z distribution is broad.

The average values of the geometric factors determined for each proton groups and for the different conformations and stoichiometries: 5-c, 6-c conformations (Fig. S13) and the 2W, 3W conformations (Fig. S14) are presented in Table 3. The differences between the 5-c and 6-c distributions arise mainly from the H1 proton group for which the distributions are
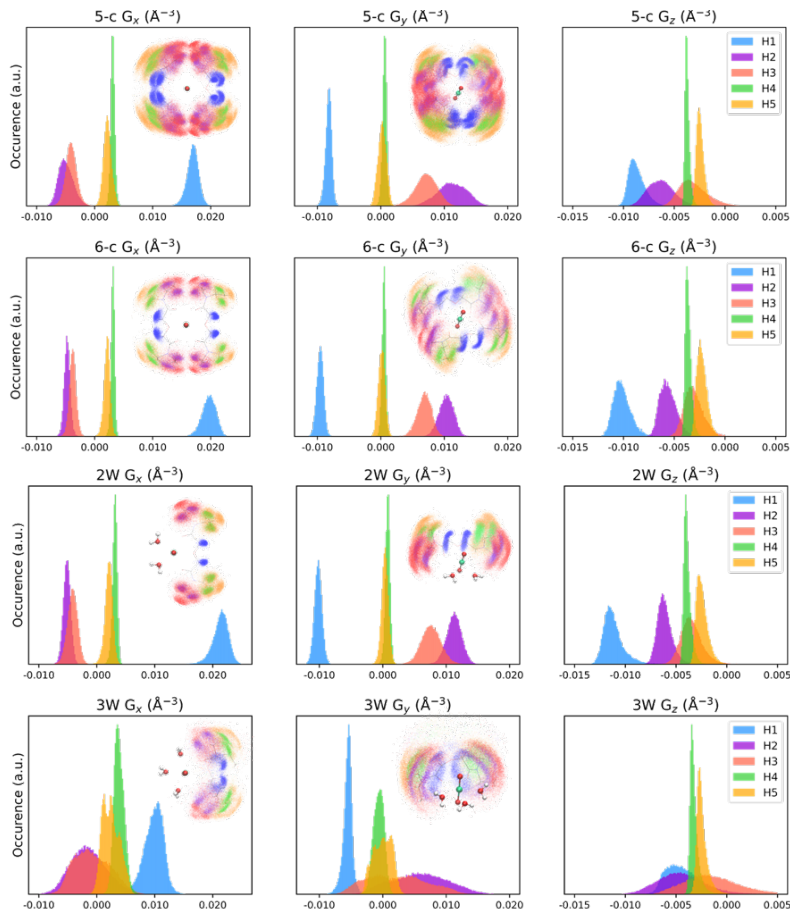
Figure 7: Distributions of the G_x, G_y and G_z geometric factors for the five- (5-c) and six-coordinated (6-c) conformations of the $[U^{VI}O_2(TEDGA)_2]^{2+}$ complex, and the 2W and 3W conformations of the $[U^{VI}O_2(TEDGA)(H_2O)_x]^{2+}$ complex. For the illustration, top and side views of the TEDGA proton atom location around the cation during the MD simulations are shown, and H1 protons are represented in blue, H2 protons in purple, H3 protons in red, H4 protons in green, and H5 protons in orange.

shifted (Fig. S13). Indeed, the absolute mean values of G_x^i, G_y^i and G_z^i (Tab. 3) are higher for the 6-c conformation than for the 5-c one, reflecting a decrease of the r distance between H1 protons and the cation, that is clearly visible on the proton localization (Fig. 7). The 5-c distributions of the H2 proton group are wider than the 6-c distributions, due to the fact that the H2 protons are more diffuse around the cation. The H3, H4 and H5 proton groups have similar distributions whatever the conformation (5-c or 6-c), these protons are less sensitive to the conformational change.

These differences described above for the 5-c and 6-c conformations of the $[U^{VI}O_2(TEDGA)_2]^{2+}$

Table 3: Average G_x^i, G_y^i and G_z^i factors determined for the $[U^{VI}O_2(TEDGA)_2]^{2+}$ six- and five-coordinated conformations, and for the $[U^{VI}O_2(TEDGA)(H_2O)_x]^{2+}$ 3W and 2W conformations ($x = 3$ and 2, respectively).

| | $[U^{VI}O_2(TEDGA)_2]^{2+}$ | | | | | |
| | five-coordinated | | | six-coordinated | | |
Proton groups	$G_x{}^a$	$G_y{}^a$	$G_z{}^a$	$G_x{}^a$	$G_y{}^a$	$G_z{}^a$
H1	16.9 ± 1.0	-8.2 ± 0.5	-8.7 ± 0.8	19.7 ± 1.2	-9.6 ± 0.5	-10.1 ± 0.9
H2	-4.9 ± 1.3	11.2 ± 2.3	-6.3 ± 1.3	-4.7 ± 0.5	10.3 ± 1.1	-5.6 ± 0.8
H3	-4.0 ± 1.0	7.1 ± 1.7	-3.1 ± 1.4	-3.8 ± 0.6	6.8 ± 1.1	-3.1 ± 0.9
H4	3.1 ± 0.3	0.6 ± 0.3	-3.7 ± 0.2	3.1 ± 0.3	0.5 ± 0.3	-3.6 ± 0.3
H5	2.2 ± 0.7	0.2 ± 0.6	-2.4 ± 0.4	2.1 ± 0.5	0.1 ± 0.5	-2.3 ± 0.5

| | $[U^{VI}O_2(TEDGA)(H_2O)_x]^{2+}$ | | | | | |
| | 2W | | | 3W | | |
Proton groups	$G_x{}^a$	$G_y{}^a$	$G_z{}^a$	$G_x{}^a$	$G_y{}^a$	$G_z{}^a$
H1	21.3 ± 1.4	-10.2 ± 0.6	-11.1 ± 1.0	9.9 ± 1.7	-5.5 ± 0.7	-4.3 ± 1.6
H2	-5.1 ± 0.6	11.2 ± 1.2	-6.1 ± 0.8	-1.4 ± 3.0	5.9 ± 4.4	-4.4 ± 2.4
H3	-4.2 ± 0.9	7.6 ± 1.6	-3.5 ± 1.1	-0.8 ± 3.1	2.2 ± 4.5	-1.4 ± 2.7
H4	3.1 ± 0.4	0.8 ± 0.4	-3.9 ± 0.4	3.8 ± 0.9	-0.6 ± 0.8	-3.2 ± 0.5
H5	2.1 ± 0.7	0.4 ± 0.5	-2.4 ± 0.6	2.5 ± 1.4	-0.1 ± 1.4	-2.4 ± 0.6

^{a} Geometric factor (10^{-3} Å^{-3}) with the standard deviation.

complex, are amplified in the G distributions between both 2W and 3W conformations, of the $[U^{VI}O_2(TEDGA)(H_2O)_x]^{2+}$ complex (Fig. 7 and Fig. S14). Indeed, the G_x^i, G_y^i and G_z^i values of the H1 proton group are twice greater for the 2W conformation compared to the 3W conformation (Tab. 3). This reflects a large distance of these protons in the 3W conformation. Almost all the distributions are wider for the 3W conformation, due to the fact that the protons take more possible positions around the cation. The distribution differences arise mainly from the H1, H2 and H3 proton groups, which are the protons the most affected by the water stoichiometries change.

More generally, in these complexes, the TEDGA molecule behaves like a flexible ligand, where its atoms can take many different positions around the cation. For the 5-c and 3W conformations, one TEDGA ether oxygen atom is not bonded to the cation, which induces

a loss of ligand stability resulting in wider distributions. The H1 proton group carried by the carbon directly bonded to the ether oxygen atom is the most affected, followed by the protons of the ethyl chain close to the cation (H2 and H3). On the contrary, the external ethyl chain (H4 and H5) is less sensitive to the U-Oether bond.

Overall, the averages of each G_z^i factor increase from the 2W to 3W conformation, and is flat for the H1, H2 and H3 proton groups showing more diffuse protons around the cation. This tendency is reminiscent of the change in the experimental chemical shift when the ratio of water concentration to complex concentration increases. The broadening of the peak correlates with that of the geometric factor distributions, and the increase in chemical shift values correlates with the increase of the geometric factors in average.

5 Determination of the χ tensor parameters

Only five characteristic chemical shifts of TEDGA are observed experimentally in the ^{1}H NMR spectrum for all the studied complexes. Each chemical shift is an average signal of the different conformations in solution, so the δ_{pc}^i of the paramagnetic complexes represents all the conformations in solution. Therefore, by taking into account the experimental χ_M and δ_{pc}^i, and the geometric factors calculated from molecular dynamics simulations, the χ tensor parameters obtained by solving the linear system composed of Eqs. 5 and 7 is an average of all the different χ tensor belonging to the species existing in solution.

5.1 An$^{\text{VI}}$ and Np$^{\text{V}}$ complexes

5.1.1 [An$^{\text{VI}}$O$_2$(TEDGA)$_2$]$^{2+}$ and [Np$^{\text{V}}$O$_2$(TEDGA)$_2$]$^+$ complexes

Table 4 shows the χ tensor parameters from the resolution of the linear system for each conformation. The Q$_{pc}$ factors (Eq. 8) are smaller for the five-coordinated conformations than for the six-coordinated one for both Pu(VI) and Np(VI) complexes 2.4 *vs.* 4.5% and 2.6 *vs.* 3.7%, respectively, while it is the reverse for the five- and six-coordinated conformation

Table 4: χ_{xx}, χ_{yy}, χ_{zz}, $\Delta\chi_{\mathrm{ax}}$, $\Delta\chi_{\mathrm{rh}}$ and Q_{pc} of the complexes calculated from the χ tensor parameters determined with the geometric factors of the five-coordinated (5-c) or 2W conformation (labeled with symbol[*]), $G_{i,j}$ with the smallest Q_{pc} (labeled with symbol[†]) and of the six-coordinated (6-c) or 3W conformation (labeled with symbol[‡]).

| | $[\mathrm{Pu^{VI}O_2(TEDGA)_2}]^{2+}$ | | | $[\mathrm{Np^{VI}O_2(TEDGA)_2}]^{2+}$ | | | $[\mathrm{Np^{V}O_2(TEDGA)_2}]^{+}$ | | |
	G_{5-c}[*]	$G_{82,18}$[†]	G_{6-c}[‡]	G_{5-c}[*]	$G_{67,33}$[†]	G_{6-c}[‡]	G_{5-c}[*]	$G_{20,80}$[†]	G_{6-c}[‡]
$\chi_{xx}{}^{a}$	5.4	5.3	4.9	2.3	2.4	2.3	4.2	3.8	3.7
$\chi_{yy}{}^{a}$	5.5	5.6	6.0	2.5	2.5	2.5	4.6	5.1	5.2
$\chi_{zz}{}^{a}$	17.7	17.7	17.7	6.7	6.7	6.7	17.3	17.3	17.3
$\Delta\chi_{\mathrm{ax}}{}^{a}$	12.3	12.3	12.2	4.3	4.3	4.2	12.9	12.8	12.8
$\Delta\chi_{\mathrm{rh}}{}^{a}$	-0.1	-0.3	-1.2	-0.2	-0.1	-0.2	-0.4	-1.2	-1.4
$Q_{\mathrm{pc}}{}^{b}$	2.4	2.3	4.5	2.6	1.9	3.7	4.2	1.8	2.0

| | $[\mathrm{Pu^{VI}O_2(TEDGA)(H_2O)_x}]^{2+}$ | | $[\mathrm{Np^{VI}O_2(TEDGA)(H_2O)_x}]^{2+}$ | |
	G_{2W}[*]	G_{3W}[‡]	G_{2W}[*]	G_{3W}[‡]
$\chi_{xx}{}^{a}$	5.1	1.8	2.2	1.0
$\chi_{yy}{}^{a}$	6.0	4.2	2.4	2.0
$\chi_{zz}{}^{a}$	17.6	22.7	6.3	7.8
$\Delta\chi_{\mathrm{ax}}{}^{a}$	12.1	19.6	3.9	6.4
$\Delta\chi_{\mathrm{rh}}{}^{a}$	-0.9	-2.4	-0.2	-1.0
$Q_{\mathrm{pc}}{}^{b}$	3.7	23.9	2.5	24.5

[a] Magnetic susceptibility (10^{-8} m^3 mol^{-1}); [b] in %.

of the Np(V) complex 4.2 *vs.* 2.0%, respectively. But the χ parameters are in same order of magnitude between the five- and six-coordinated conformations for these three complexes, especially for the χ_{zz} and $\Delta\chi_{\mathrm{ax}}$. Note that, small differences in the χ_{xx} and χ_{yy} values are observed between the conformations due to changes in the equatorial plane. This small variation of the χ parameters as a function of the conformation allows the use of a proportional geometric factor $G_{i,j}$ calculated taking into account the proportion of each conformation:

$$G_{i,j} = aG_i + bG_j, \tag{9}$$

with $0 \leq a \leq 1$, $b = 1-a$, and G_i, G_j the average geometric factors for the two conformations of the same complex (Tab. 3). The linear system made of Eqs. 5 and 7 can be solved with $G_{i,j}$ taking into account the different conformation ratios. In order to find the minimum
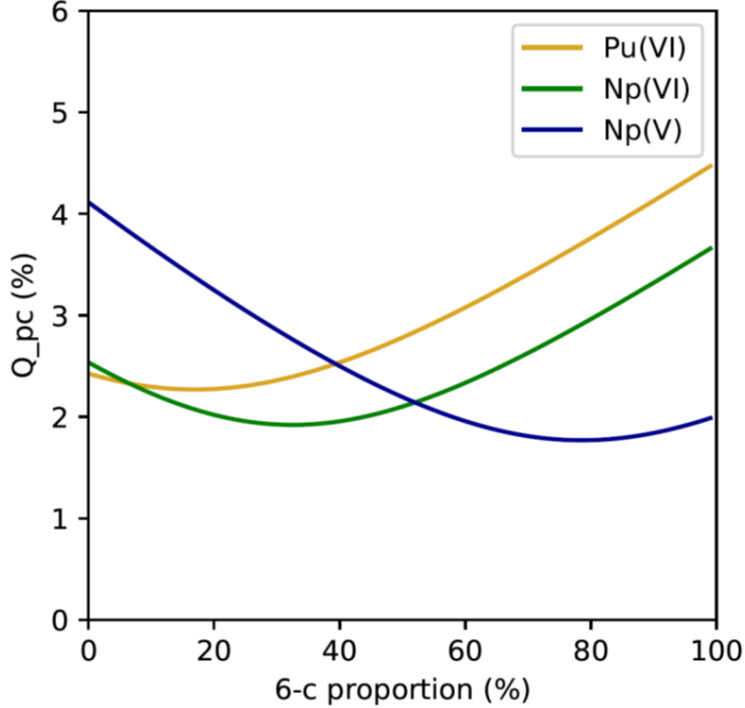
Figure 8: Q_{pc} value as a function of the proportion of the six-coordinated (6-c) conformation for $[An^{VI}O_2(TEDGA)_2]^{2+}$ (An = Pu, Np) and $[Np^V O_2(TEDGA)_2]^+$

error on the resolution of the linear system, the ratios are reached for the smallest Q_{pc} of the linear system.

The minimum Q_{pc} factor value for the $[Pu^{VI}O_2(TEDGA)_2]^{2+}$, $[Np^{VI}O_2(TEDGA)_2]^{2+}$ and $[Np^V O_2(TEDGA)_2]^+$ complexes are 18% (Q_{pc} of 2.3%), 33% (Q_{pc} of 1.9%) and 80% (Q_{pc} of 1.8%) of the six-coordinated conformation, respectively (Fig. 8). This indicates that Pu^{VI} and Np^{VI} complexes are mostly in the five-coordinated conformation, whereas Np^V is mainly in the six-coordinated conformation. This difference depending on the oxidation state can be explained by the higher distances in the NpO_2^+ first coordination shell than in the NpO_2^{2+} one because of the cation charge.[65–67] This is confirmed in MD simulations since larger U-Oe and U-Oa distances have been calculated in the case of the six-coordinated conformation (Tab. 2).

Table 5: Experimental δ_{pc}^i values for the $[Pu^{VI}O_2(TEDGA)(H_2O)_x]^{2+}$ complex with an actinide concentration of 2.5 (Syst.1) and 30 mmol L^{-1} (Syst.2), and back-calculated δ_{pc}^i with χ parameters from 2W conformation and 3W geometric factor (Syst.3). The proportion of the 2W and the 3W conformations in Syst.2 is calculated as follows: ratio = $\dfrac{(\text{Syst.2} - \text{Syst.3})}{(\text{Syst.1} - \text{Syst.3})}$

Proton group	δ_{pc}^i ^{a} Syst.1	δ_{pc}^i ^{a} Syst.2	δ_{pc}^i ^{a} Syst.3	2W proportion in Syst.2^b
H1	-52.2	-51.7	-19.8	98
H2	-36.6	-36.2	-25.0	95
H3	-19.5	-19.2	-8.0	97
H4	-21.9	-21.8	-16.1	98
H5	-12.3	-12.1	-12.4	-

^{a} in ppm; ^{b} in %.

5.1.2 $[An^{VI}O_2(TEDGA)(H_2O)_x]^{2+}$ complexes

Contrary to what was observed for the $[An^{VI}O_2(TEDGA)_2]^{2+}$ complexes, the differences in the Q_{pc} factors calculated for the $[An^{VI}O_2(TEDGA)(H_2O)_x]^{2+}$ complexes are more important between the conformations (Tab. 4). Indeed, the geometric factors of the 2W conformations are in very good agreement with the experimental shifts, with Q_{pc} values of 3.7% and 2.5% for the Pu^{VI} and Np^{VI} complexes, respectively. Furthermore, the 3W conformation does not match the experimental δ_{pc}^i, since Q_{pc} around 24% have been calculated for the two complexes. The χ parameters are also very different between both conformations, so it is impossible to use a proportional geometric factor (Eq. 9) to find the conformation ratios.

As describe before, the evolution of the chemical shifts as a function of the water concentration compared to the complex one shows that at least two conformations exist. The δ_{pc}^i of the $[Pu^{VI}O_2(TEDGA)(H_2O)_x]^{2+}$ complex for a concentration of Pu^{VI} of 2.5 (Syst.1) and 30 mmol L^{-1} (Syst.2) are given in Table 5. The water to complex ratio in Syst.1 is small and close to 3, and the geometric factors of the 2W conformation reproduces the experimental δ_{pc}^i. Therefore, it can be assumed that this sample contains almost only the 2W conformation. For Syst.2 the decrease in δ_{pc}^i proved that another conformation exists. It does not correspond to the 3W conformation alone because of the high value of the Q_{pc} value, but perhaps to a mixture of the 2W and 3W conformations. Assuming that, in the

case of actinyl cations, the χ tensor does not vary with a conformational change, the δ^i_{pc} of the 3W conformation is back-calculated using their G^i_x, G^i_y and G^i_z factors and the 2W χ parameters (Tab. 5, Syst.3), in order to compare them with the experimental ones. The proportion of each conformation has been estimated using such an approach, and we calculated a very large proportion of the 2W conformation (97% in average). The H5 G^i_x, G^i_y and G^i_z factors are close to each others, meaning that they are not affected by the conformational change. Thus, the Syst.3 δ^i_{pc} is estimated and is almost equal to the Syst.1 δ^i_{pc}. However, a δ^i_{pc} variation is still observed for the H5 proton group (0.2 ppm between Syst.1 and Syst.2), suggesting that this 3W conformation is perhaps to be rejected.

The same observations are made for the $[Np^{VI}O_2(TEDGA)(H_2O)_x]^{2+}$ complex (Tab. S7). Experimental δ^i_{pc} show that an equilibrium exists between at least two conformations, and the 2W conformation is one of them. As for the $[Pu^{VI}O_2(TEDGA)(H_2O)_x]^{2+}$ complex, the H5 proton group δ^i_{pc} always increases like the others δ^i_{pc}, despite the G^i_x, G^i_y and G^i_z factors between the 2W and 3W conformations are almost equal.

From these results, we may conclude that, for both complexes, on the contrary of the 2W conformation, the 3W conformation probably does not exist. Indeed, it could be another conformation, much similar to the 2W conformation.

5.2 χ parameters comparison

The isotropic part of the χ tensor is determined with the help of the experimental χ_M values allowing to determine χ_{xx}, χ_{yy} and χ_{zz} (Fig. 9). Note that, all determinations lead to a prolate χ tensor.

Although changes in the equatorial plane exist for the $[Pu^{VI}O_2(TEDGA)(H_2O)_x]^{2+}$ (red line in Fig. 9.a) and $[Pu^{VI}O_2(TEDGA)_2]^{2+}$ (black line in Fig. 9.a) complexes, these complexes have χ tensors very similar since the projections of the χ tensor merge together. The $\Delta\chi_{ax}$ values calculated for both complexes are close (Tab. 4). However, a slight decreasing in the $\Delta\chi_{rh}$ value is observed (from -0.3×10^{-8} to -0.9×10^{-8} m^3 mol^{-1}) certainly due to a loss of the
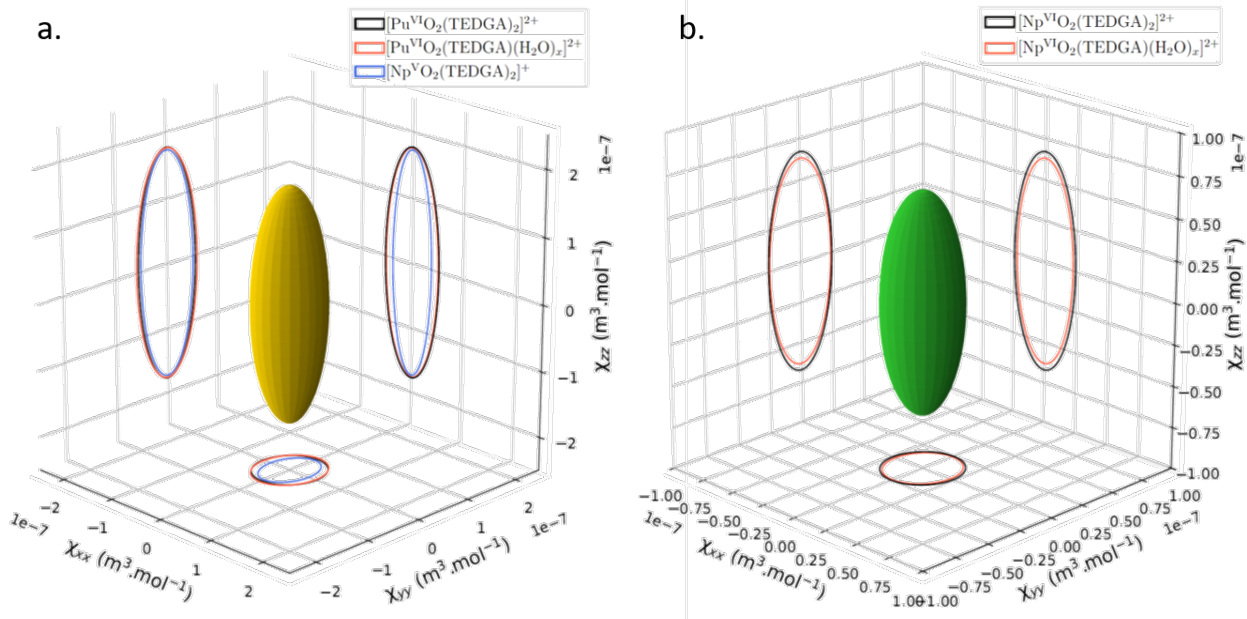
Figure 9: 3D representations of the χ tensor for the (a) $5f^2$ and (b) $5f^1$ complexes and corresponding projections on the yz, xz and xy planes.

C_2 symmetry. Comparing the $[\text{Np}^\text{V}\text{O}_2(\text{TEDGA})_2]^+$ and $[\text{Pu}^\text{VI}\text{O}_2(\text{TEDGA})_2]^{2+}$ χ tensors, we observed that the χ parameters are close, due to the same cation electronic configuration $5f^2$. Figure 9.a shows that the Np^V χ tensor is slightly smaller than the Pu^VI ones, but more rhombic along the y-axis.

Regarding the $[\text{Np}^\text{VI}\text{O}_2(\text{TEDGA})(\text{H}_2\text{O})_x]^{2+}$ complex, a slight decrease of $\Delta\chi_\text{ax}$ is observed compared to the $[\text{Np}^\text{VI}\text{O}_2(\text{TEDGA})_2]^{2+}$ one (from 4.3×10^{-8} to 3.9×10^{-8} m^3 mol^{-1}), while the $\Delta\chi_\text{rh}$ remains constant. Indeed, the χ projections of the $[\text{Np}^\text{VI}\text{O}_2(\text{TEDGA})_2]^{2+}$ complex (black line in Fig. 9.b) and the $[\text{Np}^\text{VI}\text{O}_2(\text{TEDGA})(\text{H}_2\text{O})_x]^{2+}$ complex (red line in Fig. 9.b) are less overlapped on the xz and yz planes than for the Pu^VI complexes. The $\Delta\chi_\text{ax}$ variation is explained by a more sensitivity of the Np^VI cation ($5f^1$) to the ligand field compared to the Pu^VI cation ($5f^2$).

The $\Delta\chi_\text{rh}$ value represents 2% of the $\Delta\chi_\text{ax}$ value for the $[\text{Pu}^\text{VI}\text{O}_2(\text{TEDGA})_2]^{2+}$ and the $[\text{Np}^\text{VI}\text{O}_2(\text{TEDGA})_2]^{2+}$ complexes. It increases to 5% and to 7% for the $[\text{Np}^\text{VI}\text{O}_2(\text{TEDGA})(\text{H}_2\text{O})_x]^{2+}$ and the $[\text{Pu}^\text{VI}\text{O}_2(\text{TEDGA})(\text{H}_2\text{O})_x]^{2+}$ complexes, respectively, and finally it corresponds to 9% for the $[\text{Np}^\text{V}\text{O}_2(\text{TEDGA})_2]^+$ complex. We may assume an axial tensor for the

$[\text{An}^{\text{VI}}\text{O}_2(\text{TEDGA})_2]^{2+}$ complexes, but it becomes difficult to do such an assumption for the $[\text{An}^{\text{VI}}\text{O}_2(\text{TEDGA})(\text{H}_2\text{O})_x]^{2+}$ and $[\text{Np}^{\text{V}}\text{O}_2(\text{TEDGA})_2]^{+}$ complexes.

In our previous study with the $[\text{AnO}_2(\text{DPA})_2]^{2-}$ complexes, the $\Delta\chi_{\text{ax}}$ values were 2.2×10^{-8} and 10.1×10^{-8} m^3 mol^{-1} for respectively the Np(VI) and the Pu(VI) complexes with the geometric factors arising from XRD structure.[17] The rhombic part of the tensor $\Delta\chi_{\text{rh}}$ was equal to zero. The $\Delta\chi_{\text{ax}}$ values for the 1:1 and 1:2 TEDGA complexes are 20% lower with respectively 12.3×10^{-8} and 12.1×10^{-8} m^3 mol^{-1}. This small difference can be explained by the rhombic part that is not zero due to the existence of the 5-c conformation, which does not have axial symmetry (as the 2W conformation of the $[\text{U}^{\text{VI}}\text{O}_2(\text{TEDGA})(\text{H}_2\text{O})_x]^{2+}$ complex). Indeed, the loss of the axial symmetry leads to a modification of the χ tensor, but minor in the case of the Pu$^{\text{VI}}$ cation. On the contrary, the Np$^{\text{VI}}$ TEDGA complexes show highest $\Delta\chi_{\text{ax}}$ values, almost double, with 4.3 and 3.9 for respectively the 1:1 and 1:2 complexes. The χ tensor is more impacted by the ligand modification in the case of the Np$^{\text{VI}}$ cation.

For the $[\text{Np}^{\text{V}}\text{O}_2(\text{TEDGA})_2]^{+}$ complex, the $\Delta\chi_{\text{ax}}$ value was found to be 10% higher than in the present study. Furthermore, a $\Delta\chi_{\text{rh}}$ value representing around 10% of the $\Delta\chi_{\text{ax}}$ value was found in both studies. However, it has to be reminded that the diamagnetic reference use for the $[\text{Np}^{\text{V}}\text{O}_2(\text{TEDGA})_2]^{+}$ complex was the $[\text{U}^{\text{VI}}\text{O}_2(\text{TEDGA})_2]^{2+}$ complex, while it would have be the $[\text{Pa}^{\text{V}}\text{O}_2(\text{TEDGA})_2]^{+}$, but unfortunately this element (Pa$^{\text{V}}$) was not available in our laboratory.

Both methods using the geometric factor for the determination of the χ parameters lead to similar results. Indeed, the structures found are close, *i.e.*, the position of the protons around the cation are similar, despite a modification of the cation equatorial plane resulting from different coordination modes of the ligands (five- and six-coordinated complexes) or the presence of water molecules.

6 Conclusions

In the present study, we have demonstrated the effectiveness of coupling molecular dynamics simulations with pNMR for the determination of the structural properties of An^V (An = Np) and An^{VI} (An = U, Pu, and Np) complexes with TEDGA ligands. Indeed, molecular dynamics allows to simulate all possible conformations that exist in solution, implying thus a better depiction of the chemical system and of the calculation of geometric factors needed for the determination of the χ tensor. Nevertheless, the conformations observed in MD simulation must be analyzed separately, in order to verify their agreement with the experimental δ^i_{pc}.

Molecular dynamics simulations of $[U^{VI}O_2(TEDGA)(H_2O)_x]^{2+}$ and $[U^{VI}O_2(TEDGA)_2]^{2+}$ complexes in acetonitrile have shown that two different conformations exist for both complexes, which was not expected from NMR experiments since only one set of five proton peaks was observed. Indeed, NMR spectroscopy did not allow to distinguish between both conformations of the $[An^{VI}O_2(TEDGA)_2]^{2+}$ complex due to a fast conformation exchange. The existence of these two conformations has been confirmed by EXAFS experiments since the adjustment of the EXAFS spectra was not possible taking into account only one of the conformations. Moreover, the resolution of the linear system allows to calculate χ tensor parameters with a very good accuracy (small Q_{pc} values), which confirms the good agreement between the molecular dynamics simulations and the pNMR experiments.

Concerning the $[An^{VI}O_2(TEDGA)(H_2O)_x]^{2+}$ complexes, the NMR spectroscopy showed the existence of two different conformations in solution, their proportion depending on the water concentration. From molecular dynamics simulations, we observed that the conformations, both with a coordination number of five, have either two or three water molecules in the cation first coordination sphere. However, comparing the results with the experimental δ^i_{pc}, it appears that the conformation with three water molecules did not properly reproduce the experiments, while the one with two water molecules is in good agreement with the pNMR results.

However, one has to remember that with actinide cations, each conformation of the complex has its own χ tensor, so there are as many different tensors as images of the complex. In this work, an average set of χ tensor parameters has been determined for all structures having the same conformation.

We confirm and demonstrate that the magnetic susceptibility anisotropy remained in the same magnitude order due the -yle bond. Indeed, a modification of the equatorial plane (replacement of a TEDGA molecule by water molecules) affects few the χ parameters of the complex. As expected, this change is slightly more pronounced for the $5f^1$ complexes. Based on these good results obtained from molecular dynamics and the use of the actinyl cations as paramagnetic probe, we are confident in studies of more flexible ligands and of interest in biochemistry for example.

Acknowledgement

Supporting Information Available

The following files are available free of charge.

- Force field parameters used for the MD simulations (Tables S1-S5 and Figure S1)

- ^{1}H NMR spectra (Figures S2, S3 and S4)

- Magnetic susceptibility determination by Evans method (Figures S5 to S9)

- Distributions of the complexes life-times (Figure S10)

- Radial distributions functions issued from MD simulations and the EXAFS metrics parameters (Figure S11)

- Experimental and theoretical EXAFS signals (Figure S12)

- Distributions of the G_x, G_y and G_z factors (Figures S13 and S14)

- ^{1}H chemical shifts (Tables S6 and S7)

References

(1) Kato, K.; Yamaguchi, T. Paramagnetic NMR Probes for Characterization of the Dynamic Conformations and Interactions of Oligosaccharides. *Glycoconj. J.* **2015**, *32*, 505–513.

(2) Nitsche, C.; Otting, G. Pseudocontact Shifts in Biomolecular NMR Using Paramagnetic Metal Tags. *Prog. Nucl. Magn. Reson. Spectrosc.* **2017**, *98-99*, 20–49.

(3) Joss, D.; Häussinger, D. Design and Applications of Lanthanide Chelating Tags for Pseudocontact Shift NMR Spectroscopy With Biomacromolecules. *Prog. Nucl. Magn. Reson. Spectrosc.* **2019**, *114-115*, 284–312.

(4) Bertini, I.; Janik, M. B. L.; Lee, Y.-M.; Luchinat, C.; Rosato, A. Magnetic Susceptibility Tensor Anisotropies for a Lanthanide Ion Series in a Fixed Protein Matrix. *J. Am. Chem. Soc.* **2001**, *123*, 4181–4188.

(5) Jensen, M. R.; Hansen, D. F.; Ayna, U.; Dagil, R.; Hass, M. A. S.; Christensen, H. E. M.; Led, J. J. On the Use of Pseudocontact Shifts in the Structure Determination of Metalloproteins. *Magn. Reson. Chem.* **2006**, *44*, 294–301.

(6) Pintacuda, G.; John, M.; Su, X.-C.; Otting, G. NMR Structure Determination of Protein-Ligand Complexes by Lanthanide Labeling. *Acc. Chem. Res.* **2007**, *40*, 206–212.

(7) Graham, B.; Loh, C. T.; Swarbrick, J. D.; Ung, P.; Shin, J.; Yagi, H.; Jia, X.; Chhabra, S.; Barlow, N.; Pintacuda, G.; Huber, T.; Otting, G. DOTA-Amide Lanthanide Tag for Reliable Generation of Pseudocontact Shifts in Protein NMR Spectra. *Bioconjugate Chem.* **2011**, *22*, 2118–2125.

(8) Schmitz, C.; Vernon, R.; Otting, G.; Baker, D.; Huber, T. Protein Structure Determination from Pseudocontact Shifts Using ROSETTA. *J. Mol. Biol.* **2012**, *416*, 668–677.

(9) Yagi, H.; Pilla, K. B.; Maleckis, A.; Graham, B.; Huber, T.; Otting, G. Three-Dimensional Protein Fold Determination from Backbone Amide Pseudocontact Shifts Generated by Lanthanide Tags at Multiple Sites. *Structure* **2013**, *21*, 883–890.

(10) Saio, T.; Ishimori, K. Accelerating Structural Life Science by Paramagnetic Lanthanide Probe Methods. *Biochim. Biophys. Acta - Gen. Subj.* **2020**, *1864*, 129332.

(11) Autillo, M.; Guerin, L.; Dumas, T.; Grigoriev, M. S.; Fedoseev, A. M.; Cammelli, S.; Solari, P. L.; Guillaumont, D.; Guilbaud, P.; Moisy, P.; Bolvin, H.; Berthon, C. Insight of the Metal–Ligand Interaction in f-Element Complexes by Paramagnetic NMR Spectroscopy. *Chem. – Eur. J.* **2019**, *25*, 4435–4451.

(12) Runde, W.; Reilly, S.; Neu, M. Spectroscopic Investigation of the Formation of PuO_2Cl^+ and PuO_2Cl_2 in NaCl Solutions and Application for Natural Brine Solutions. *Geochim. Cosmochim. Acta* **1999**, *63*, 3443–3449.

(13) Szabó, Z.; Toraishi, T.; Vallet, V.; Grenthe, I. Solution Coordination Chemistry of Actinides: Thermodynamics, Structure and Reaction Mechanisms. *Coord. Chem. Rev.* **2006**, *250*, 784–815.

(14) Jeanson, A.; Berthon, C.; Coantic, S.; Den Auwer, C.; Floquet, N.; Funke, H.; Guillaneux, D.; Hennig, C.; Martinez, J.; Moisy, P.; Petit, S.; Proux, O.; Quémeneur, E.; Solari, P. L.; Subra, G. The Role of Aspartyl-Rich Pentapeptides in Comparative Complexation of Actinide(IV) and Iron(III). Part 1. *New J. Chem.* **2009**, *33*, 976.

(15) Zhou, L.; Bosscher, M.; Zhang, C.; Özçubukçu, S.; Zhang, L.; Zhang, W.; Li, C. J.; Liu, J.; Jensen, M. P.; Lai, L.; He, C. A Protein Engineered to Bind Uranyl Selectively and with Femtomolar Affinity. *Nature Chemistry* **2014**, *6*, 236–241.

(16) Martin, N. P.; Volkringer, C.; Henry, N.; Duval, S.; Mara, D.; Van Deun, R.; Loiseau, T. Molecular Assemblies of a Series of Mixed Tetravalent Uranium and Trivalent Lanthanide Complexes Associated with the Dipicolinate Ligand, in Aqueous Medium. *Cryst. Growth Des* **2018**, *18*, 2165–2179.

(17) Autillo, M.; Islam, M. A.; Héron, J.; Guérin, L.; Acher, E.; Tamain, C.; Illy, M.-C.; Moisy, P.; Colineau, E.; Griveau, J.-C.; Berthon, C.; Bolvin, H. Temperature Dependence of ^{1}H Paramagnetic Chemical Shifts in Actinide Complexes, Beyond Bleaney's Theory: The $An^{VI}O_2^{2+}$–Dipicolinic Acid Complexes (An=Np, Pu) as an Example. *Chem. – Eur. J.* **2021**, *27*, 7138–7153.

(18) Sasaki, Y.; Suzuki, H.; Sugo, Y.; Kimura, T.; Choppin, G. R. New Water-Soluble Organic Ligands for Actinide Cations Complexation. *Chem. Lett.* **2006**, *35*, 256–257.

(19) Charbonnel, M.-C.; Berthon, C.; Berthon, L.; Boubals, N.; Burdet, F.; Duchesne, M.-T.; Guilbaud, P.; Mabille, N.; Petit, S.; Zorz, N. Complexation of Ln(III) and Am(III) With the Hydrosoluble TEDGA: Speciation and Thermodynamics Studies. *Procedia Chem.* **2012**, *7*, 20–26.

(20) Reilly, S. D.; Gaunt, A. J.; Scott, B. L.; Modolo, G.; Iqbal, M.; Verboom, W.; Sarsfield, M. J. Plutonium(IV) Complexation by Diglycolamide Ligands – Coordination Chemistry Insight Into TODGA-Based Actinide Separations. *Chem. Commun.* **2012**, *48*, 9732.

(21) Lange, S.; Wilden, A.; Modolo, G.; Sadowski, F.; Gerdes, M.; Bosbach, D. Direct Selective Extraction of Trivalent Americium from PUREX Raffinate Using a Combination

of CyMe$_4$BTPhen and TEDGA – A Feasibility Study. *Solvent Extr. Ion Exch.* **2017**, *35*, 161–173.

(22) Bertini, I.; Luchinat, C.; Parigi, G. Magnetic Susceptibility in Paramagnetic NMR. *Prog. Nucl. Magn. Reson. Spectrosc.* **2002**, *40*, 249–273.

(23) Banci, L.; Bertini, I.; Bren, K. L.; Cremonini, M. A.; Gray, H. B.; Luchinat, C.; Turano, P. The Use of Pseudocontact Shifts to Refine Solution Structures of Paramagnetic Metalloproteins: Met80Ala Cyano-Cytochrome C as an Example. *J. Bio. Inorg. Chem.* **1996**, *1*, 117–126.

(24) Zhang, Y.; Yamamoto, S.; Yamaguchi, T.; Kato, K. Application of Paramagnetic NMR-Validated Molecular Dynamics Simulation to the Analysis of a Conformational Ensemble of a Branched Oligosaccharide. *Molecules* **2012**, *17*, 6658–6671.

(25) Hass, M. A.; Ubbink, M. Structure Determination of Protein – Protein Complexes with Long-Range Anisotropic Paramagnetic NMR Restraints. *Curr. Opin. Struct. Biol.* **2014**, *24*, 45–53.

(26) Denis-Quanquin, S.; Bartocci, A.; Szczepaniak, F.; Riobé, F.; Maury, O.; Dumont, E.; Giraud, N. Capturing the Dynamic Association Between a Tris-Dipicolinate Lanthanide Complex and a Decapeptide: a Combined Paramagnetic NMR and Molecular Dynamics Exploration. *Phys. Chem. Chem. Phys.* **2021**, *23*, 11224–11232.

(27) Sala, D.; Giachetti, A.; Luchinat, C.; Rosato, A. A Protocol for the Refinement of NMR Structures Using Simultaneously Pseudocontact Shift Restraints from Multiple Lanthanide Ions. *J. Biomol. NMR* **2016**, *66*, 175–185.

(28) Guilbaud, P.; Wipff, G. Hydration of Uranyl (UO_2^{2+}) Cation and its Nitrate Ion and 18-Crown-6 Adducts Studied by Molecular Dynamics Simulations. *J. Phys. Chem.* **1993**, *97*, 5685–5692.

(29) Ye, X.; Smith, R. B.; Cui, S.; de Almeida, V.; Khomami, B. Influence of Nitric Acid on Uranyl Nitrate Association in Aqueous Solutions: A Molecular Dynamics Simulation Study. *Solvent Extr. Ion Exch.* **2010**, *28*, 1–18.

(30) Bühl, M.; Wipff, G. Insights Into Uranyl Chemistry from Molecular Dynamics Simulations. *ChemPhysChem.* **2011**, *12*, 3095–3105.

(31) Pérez-Conesa, S.; Torrico, F.; Martínez, J. M.; Pappalardo, R. R.; Marcos, E. S. A Hydrated Ion Model of UO_2^{2+} in Water: Structure, Dynamics, and Spectroscopy From Classical Molecular Dynamics. *J. Chem. Phys.* **2016**, *145*, 224502.

(32) Lahrouch, F.; Chamayou, A. C.; Creff, G.; Duvail, M.; Hennig, C.; Rodriguez, M. J. L.; Den Auwer, C.; Giorgio, C. D. A Combined Spectroscopic/Molecular Dynamic Study for Investigating a Methyl-Carboxylated PEI as a Potential Uranium Decorporation Agent. *Inorg. Chem.* **2017**, *56*, 1300–1308.

(33) Newcomb, K.; Tiwari, S. P.; Rai, N.; Maginn, E. J. A Molecular Dynamics Investigation of Actinyl – Ligand Speciation in Aqueous Solution. *Phys. Chem. Chem. Phys.* **2018**, *20*, 15753–15763.

(34) Paquet, A.; Diat, O.; Berthon, L.; Guilbaud, P. Aggregation in Organic Phases After Solvent Extraction of Uranyl Nitrate: X-Ray Scattering and Molecular Dynamic Simulations. *J. Mol. Liq.* **2019**, *277*, 22–35.

(35) Duvail, M.; Dumas, T.; Paquet, A.; Coste, A.; Berthon, L.; Guilbaud, P. UO_2^{2+} Structure in Solvent Extraction Phases Resolved at Molecular and Supramolecular Scales: a Combined Molecular Dynamics, EXAFS and SWAXS Approach. *Phys. Chem. Chem. Phys.* **2019**, *21*, 7894–7906.

(36) Maerzke, K. A.; Goff, G. S.; Runde, W. H.; Schneider, W. F.; Maginn, E. J. Structure and Dynamics of Uranyl(VI) and Plutonyl(VI) Cations in Ionic Liquid/Water Mixtures via Molecular Dynamics Simulations. *J. Phys. Chem. B* **2013**, *117*, 10852–10868.

(37) Raposo-Hernández, G.; Martínez, J. M.; Pappalardo, R. R.; Den Auwer, C.; Marcos, E. S. A Coupled EXAFS-Molecular Dynamics Study on PuO_2^+ and NpO_2^+ Hydration: The Importance of Electron Correlation in Force-Field Building. *Inorg. Chem.* **2022**, *61*, 8703–8714.

(38) Spezia, R.; Migliorati, V.; D'Angelo, P. On the Development of Polarizable and Lennard-Jones Force Fields to Study Hydration Structure and Dynamics of Actinide(III) Ions Based on Effective Ionic Radii. *J. Chem. Phys.* **2017**, *147*, 161707.

(39) Réal, F.; Trumm, M.; Vallet, V.; Schimmelpfennig, B.; Masella, M.; Flament, J.-P. Quantum Chemical and Molecular Dynamics Study of the Coordination of Th(IV) in Aqueous Solvent. *J. Phys. Chem. B* **2010**, *114*, 15913–15924.

(40) Priest, C.; Li, B.; Jiang, D.-e. Uranyl–Glutardiamidoxime Binding from First-Principles Molecular Dynamics, Classical Molecular Dynamics, and Free-Energy Simulations. *Inorg. Chem.* **2017**, *56*, 9497–9504.

(41) Kumar, N.; Servis, M. J.; Clark, A. E. Uranyl Speciation in the Presence of Specific Ion Gradients at the Electrolyte/Organic Interface. *Solvent Extr. Ion Exch.* **2021**, *40*, 165–187.

(42) Farnan, I.; Berthon, C. In *SPR-Nuclear Magnetic Resonance*, 1st ed.; Ramesh, V., Ed.; Specialist Periodical Reports (Book 45); Royal Society of Chemistry; Gld edition (May 11, 2016), 2016; Vol. 45; Chapter 3.

(43) Iverson, D. OpenVnmrJ, version 2.1.A. 2020; `https://openvnmrj.org`.

(44) Evans, D. The Determination of the Paramagnetic Susceptibility of Substances in Solution by Nuclear Magnetic Resonance. *J. Chem. Soc.* **1959**, 2003–2005.

(45) LLorens, I.; Solari, P. L.; Sitaud, B.; Bes, R.; Cammelli, S.; Hermange, H.; Othmane, G.; Safi, S.; Moisy, P.; Wahu, S.; Bresson, C.; Schlegel, M. L.; Menut, D.; Bechade, J.-L.;

Martin, P.; Hazemann, J.-L.; Proux, O.; Den Auwer, C. X-ray Absorption Spectroscopy Investigations on Radioactive Matter Ssing MARS Beamline at SOLEIL Synchrotron. *Radiochim. Acta* **2014**, *102*, 957–972.

(46) Ravel, B.; Newville, M. ATHENA, ARTEMIS, HEPHAESTUS: Data Analysis for X-ray Absorption Spectroscopy using IFEFFIT. *J. Synchrotron Radiat.* **2005**, *12*, 537–541.

(47) Rehr, J. J.; Albers, R. C. Theoretical Approaches to X-Ray Absorption Fine Structure. *Rev. Mod. Phys.* **2000**, *72*, 621–654.

(48) Case, D. A.; Belfon, K.; Ben-Shalom, I. Y.; Brozell, S. R.; Cerutti, D. S.; Cheatham, III, T. E.; Cruzeiro, V. W. D.; Darden, T. A.; Duke, R. E.; Giambasu, G.; Gilson, M. K.; Gohlke, H.; Goetz, A. W.; Harris, R.; Izadi, S.; Izmailov, S. A.; Kasavajhala, K.; Kovalenko, A.; Krasny, R.; Kurtzman, T.; Lee, T. S.; LeGrand, S.; Li, P.; Lin, C.; Liu, J.; Luchko, T.; Luo, R.; Man, V.; Merz, K. M.; Miao, Y.; Mikhailovskii, O.; Monard, G.; Nguyen, H.; Onufriev, A.; Pan, F.; Pantano, S.; Qi, R.; Roe, D. R.; Roitberg, A.; Sagui, C.; Schott-Verdugo, S.; Shen, J.; Simmerling, C. L.; Skrynnikov, N. R.; Smith, J.; Swails, J.; Walker, R. C.; Wang, J.; Wilson, L.; Wolf, R. M.; Wu, X.; Xiong, Y.; Xue, Y.; York, D. M.; Kollman, P. A. AMBER 2020. 2020; University of California, San Francisco.

(49) Darden, T.; York, D.; Pedersen, L. Particle Mesh Ewald: An $N \cdot \log(N)$ Method for Ewald Sums in Large Systems. *J. Chem. Phys.* **1993**, *98*, 10089–10092.

(50) Caldwell, J. W.; Kollman, P. A. Structure and Properties of Neat Liquids Using Nonadditive Molecular Dynamics: Water, Methanol, and N-Methylacetamide. *J. Phys. Chem.* **1995**, *99*, 6208–6219.

(51) Meng, E. C.; Kollman, P. A. Molecular Dynamics Studies of the Properties of Water around Simple Organic Solutes. *J. Phys. Chem.* **1996**, *100*, 11460–11470.

(52) Howard, A. E.; Cieplak, P.; Kollman, P. A. A Molecular Mechanical Model That Reproduces the Relative Energies for Chair and Twist-Boat Conformations of 1,3-Dioxanes. *J. Comput. Chem.* **1995**, *16*, 243–261.

(53) Nikitin, A. M.; Lyubartsev, A. P. New Six-Site Acetonitrile Model for Simulations of Liquid Acetonitrile and its Aqueous Mixtures. *J. Comput. Chem.* **2007**, *28*, 2020–2026.

(54) Case, D. A.; Cheatham, T. E.; Darden, T.; Gohlke, H.; Luo, R.; Merz, K. M.; Onufriev, A.; Simmerling, C.; Wang, B.; Woods, R. J. The Amber Biomolecular Simulation Programs. *J. Comput. Chem.* **2005**, *26*, 1668–1688.

(55) Frisch, M. J.; Trucks, G. W.; Schlegel, H. B.; Scuseria, G. E.; Robb, M. A.; Cheeseman, J. R.; Scalmani, G.; Barone, V.; Mennucci, B.; Petersson, G. A.; Nakatsuji, H.; Caricato, M.; Li, X.; Hratchian, H. P.; Izmaylov, A. F.; Bloino, J.; Zheng, G.; Sonnenberg, J. L.; Hada, M.; Ehara, M.; Toyota, K.; Fukuda, R.; Hasegawa, J.; Ishida, M.; Nakajima, T.; Honda, Y.; Kitao, O.; Nakai, H.; Vreven, T.; Montgomery, J. A., Jr.; Peralta, J. E.; Ogliaro, F.; Bearpark, M.; Heyd, J. J.; Brothers, E.; Kudin, K. N.; Staroverov, V. N.; Kobayashi, R.; Normand, J.; Raghavachari, K.; Rendell, A.; Burant, J. C.; Iyengar, S. S.; Tomasi, J.; Cossi, M.; Rega, N.; Millam, J. M.; Klene, M.; Knox, J. E.; Cross, J. B.; Bakken, V.; Adamo, C.; Jaramillo, J.; Gomperts, R.; Stratmann, R. E.; Yazyev, O.; Austin, A. J.; Cammi, R.; Pomelli, C.; Ochterski, J. W. et al. Gaussian 09 Revision B.01. 2009; `http://www.gaussian.com/`, Gaussian Inc. Wallingford CT.

(56) Bayly, C. I.; Cieplak, P.; Cornell, W.; Kollman, P. A. A Well-Behaved Electrostatic Potential Based Method Using Charge Restraints for Deriving Atomic Charges: the RESP Model. *J. Phys. Chem.* **1993**, *97*, 10269–10280.

(57) Cornell, W. D.; Cieplak, P.; Bayly, C. I.; Gould, I. R.; Merz, K. M.; Ferguson, D. M.; Spellmeyer, D. C.; Fox, T.; Caldwell, J. W.; Kollman, P. A. A Second Generation

Force Field for the Simulation of Proteins, Nucleic Acids, and Organic Molecules. *J. Am. Chem. Soc.* **1995**, *117*, 5179–5197.

(58) Duvail, M.; Villard, A.; Nguyen, T.-N.; Dufrêche, J.-F. Thermodynamics of Associated Electrolytes in Water: Molecular Dynamics Simulations of Sulfate Solutions. *J. Phys. Chem. B* **2015**, *119*, 11184–11195.

(59) Roe, D. R.; Cheatham, T. E. PTRAJ and CPPTRAJ: Software for Processing and Analysis of Molecular Dynamics Trajectory Data. *J. Chem. Theory Comput.* **2013**, *9*, 3084–3095.

(60) Bertini, I.; Luchinat, C.; Parigi, G.; Ravera, E. *Solution NMR of Paramagnetic Molecules*; Elsevier, 2017; pp 1–49.

(61) Branch, M. A.; Coleman, T. F.; Li, Y. A Subspace, Interior, and Conjugate Gradient Method for Large-Scale Bound-Constrained Minimization Problems. *SIAM J. Sci. Comput.* **1999**, *21*, 1–23.

(62) Cornilescu, G.; Marquardt, J. L.; Ottiger, M.; Bax, A. Validation of Protein Structure from Anisotropic Carbonyl Chemical Shifts in a Dilute Liquid Crystalline Phase. *J. Am. Chem. Soc.* **1998**, *120*, 6836–6837.

(63) Impey, R. W.; Madden, P. A.; McDonald, I. R. Hydration and Mobility of Ions in Solution. *J. Phys. Chem.* **1983**, *87*, 5071–5083.

(64) Duvail, M.; Souaille, M.; Spezia, R.; Cartailler, T.; Vitorge, P. Pair interaction potentials with explicit polarization for molecular dynamics simulations of La3+ in bulk water. *J. Chem. Phys.* **2007**, *127*, 034503.

(65) Hay, P. J.; Martin, R. L.; Schreckenbach, G. Theoretical Studies of the Properties and Solution Chemistry of $AnO_2{}^{2}+$ and AnO_2^+ Aquo Complexes for An = U, Np, and Pu. *J. Phys. Chem. A* **2000**, *104*, 6259–6270.

(66) Lan, J.-H.; Wang, C.-Z.; Wu, Q.-Y.; Wang, S.-A.; Feng, Y.-X.; Zhao, Y.-L.; Chai, Z.-F.; Shi, W.-Q. A Quasi-Relativistic Density Functional Theory Study of the Actinyl(VI, V) (An = U, Np, Pu) Complexes With a Six-Membered Macrocycle Containing Pyrrole, Pyridine, and Furan Subunits. *J. Phys. Chem. A* **2015**, *119*, 9178–9188.

(67) Pérez-Conesa, S.; Torrico, F.; Martínez, J. M.; Pappalardo, R. R.; Marcos, E. S. A General Study of Actinyl Hydration by Molecular Dynamics Simulations Using *Ab Initio* Force Fields. *J. Chem. Phys.* **2019**, *150*, 104504.

TOC Graphic

$$\delta_{pc} = \frac{10^6}{12\pi N_A}\left[\chi_{xx}G_x + \chi_{yy}G_y + \chi_{zz}G_z\right]$$

Chemical shift (ppm)